Faculty of Mechanical, Maritime and Materials Engineering (3mE)

Adverse pressure gradient flows and their influence on boundary layer flashback

Master thesis

Akhil Penmathsa

Thesis Comittee
Prof.dr.ir. Sikke Klein
Dr.ir. R. Pecnik
Prof.dr.ir. B.J. Boersma

Final version

Delft, January 2021

Abstract

Flame flashback is a failure mode in the operation of lean premixed combustion system. Due to higher flame speeds and lower quenching distances, hydrogen-rich fuel mixtures are prone to boundary layer flashback (BLF), where mixture flow speeds are low compared to the local flow velocity. Research at TU Munich (Eichler 2011) has resulted in new insights into the mechanism of BLF in confined geometries, revealing a strong interaction between the incoming flowfield and the flame. BLF occurs due to flow separation in confined geometries. Studies from Gruber (2012) also confirmed this effect and it was hypothesized that Darrieus Landau (DL) instability can cause the flow separation. Studies from TU Munich also showed increased flashback propensity in the presence of adverse pressure gradient.

In this thesis, detailed study of the flow structure in the diffuser is performed. LES simulations are performed for the channel and diffuser and are validated with the results from the literature. First a comparison of subgrid scale models is performed for the channel case. Then, a detailed study of the time resolved structure for the channel and diffuser is performed with the two point correlations and cumulative distribution functions of instantaneous velocity. It has been observed that the turbulent structures are shorter in the diffuser compared to the channel. Then, the relevance of DL instability is investigated in the channel and diffuser geometries. It has been found that DL instability is more prevalent in the diffuser due to decrease in the turbulent frequencies. Together these effects could be the reason for the increased flashback propensity observed in adverse pressure gradient flows.

Preface

I want to thank Rene and Sikke for the trust they had in me and allowing me to develop the project at my own pace and also taking part in weekly discussions and meetings. I got to learn a lot both technically and personally from them in the duration of project.

I also want to thank Mathieu for providing me different ideas on approaching the simulation problem and also on using the CFD software.

I am also grateful for the support of my family and friends across the globe. Without their support I could not have gone through this period of uncertainity without any hinderances.

I would also like to thank all the frontline service workers and healthline workers for keeping us safe and out of harms way during the pandemic.

Akhil

Delft, January 2021

Contents

List of Figures

List of Tables

Chapter 1

Introduction

According to the latest report of the Intergovernmental Panel on Climate Change (IPCC) [5], the period between 1983 and 2012 is the warmest 30-year period of the last 1400 years. The warming of the atmosphere is happening due to the enormous amounts of greenhouse gases emitted during the industrial era. Figure 1.1 shows the global temperature, global sea level, averaged greenhouse gas emissions and anthropogenic CO_2 emissions. We can clearly see a causal relationship between greenhouse gas emissions and increased global temperatures and sea level rises. The figure also shows that most of the resulting increase in the greenhouse gas emission is due to human activities.

Due to the impending effects of climate change, many sectors in the society are opting for sustainable power generation. Among them solar and wind are gaining interest due to their 100% renewable energy generation capabilities and also maturing technologies. However the power generation due to solar and wind are subject to intermittency and are not reliable since they highly depend on the weather conditions. This requires the use of intermediate power source to store the excess energy generated by the renewable sources during favourable weather conditions and use this energy when the supply of power cannot meet the demand. Batteries are one example of an intermediate energy storage system. Batteries have very low power density and in order to meet the power demands, we would require very large increase in the current battery capacity.

Hydrogen has been gaining interest as this intermediate power source since it can produce power by using it in the fuel cells and also burning it in the gas turbines. Gas turbines can balance the intermittent power requirements well due to their fast startup times, high efficiency and high turn down ratios. Hydrogen can be produced by electrolysis and steam reforming of the natural gas. The existing natural gas network can also be used to transport hydrogen, prompting a reduction in the investment.

Stable burning of 100 percent hydrogen or hydrogen-rich mixtures is difficult. Hydrogen burns much quicker than standard fuels like natural gas. It also has higher flame temperature and is more resistant to quenching. These properties contribute to a higher chance of a phenomenon called as flame flashback. Since flashback is one of the failure modes of gas turbine operation, proper design accounting for this effect is essential.

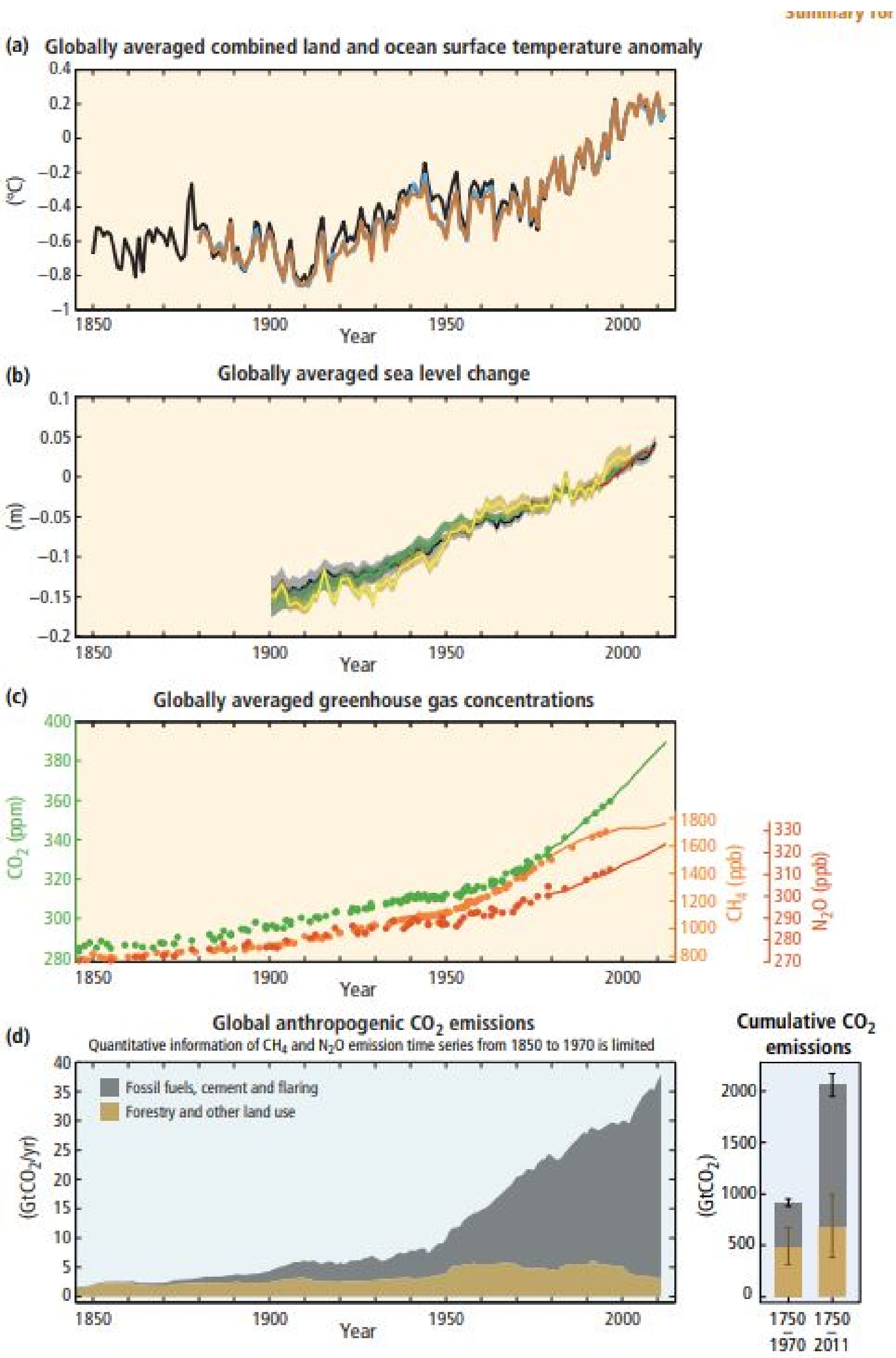

Figure 1.1: The complex relationship between global temperature rise, global sea level rise and emissions. Source : IPCC [5]

1.1 Thesis Outline

The current study focuses on the investigation of the flow structure in the diffuser and its influence on the flashback propensity. Chapter two details the literature study on the topic. The literature study is divided into two parts. The first part details the studies on boundary layer flashback with relevance to hydrogen combustion. The second part of the study focuses on the effect of adverse pressure gradient on the flow structure of turbulent boundary layers. Chapter three gives description of the numerical modeling used in the study. Chapter four and five give the setup and results of 0 degree channel and 2 degree diffuser respectively. Chapter six gives the discussion of the results followed by the conclusions and recommendations in chapter seven.

Chapter 2

Literature Survey

2.1 Flashback mechanisms in Premixed Flames

Flashback occurs when the flame front propagates against the mean flow. Flashback can cause the flame front to propagate into the premixer section of the gas turbines. Since the premixer section is not designed for the high temperature conditions of the flame, this can cause a failure in the operation of gas turbines.

In general, flame flashback occurs in following four mechanisms [6]:

- **Flashback in core flow:** When incoming bulk flow velocity falls below the flame speed, flashback in core flow occurs. This mechanism of flashback is characterized by the kinematic balance between the bulk flow velocity and the flame speed. This is negligible in normal operating conditions because the bulk flow velocity generally exceeds the flame speed.

- **Flashback due to Combustion instabilities :** This phenomenon is characterized by the complex interaction between the acoustic modes, heat release and the flow field structure. These interactions can cause the flow to stagnate and hence increase propensity of the upward propagation of the flame.

- **Combustion induced vortex breakdown :** This mechanism is specific to swirl stabilized burners. This phenomenon occurs due to upstream propagation of the recirculation zone due to pressure rise associated with the flame. This causes the vortex to breakdown in the duct and hence cause flashback into the premixer section. In general, increased hydrogen content can increase the propensity of this mechanism to occur.

- **Boundary Layer Flashback :** Due to the no slip condition at the wall, flow velocity near the wall is very low compared to the velocity in the core region. Hence there is a chance for the flame speed to exceed flow velocity in these regions and hence cause flashback to occur at a certain distance from the wall. In general this effect is negligible in hydrocarbon fuel combustion and becomes relevant in high hydrogen content fuels due to a significant increase in the flame speed due to hydrogen combustion.

Hydrogen combustion is more susceptible to flashback than hydrocarbon combustion. Hydrogen is more reactive than hydrocarbon fuels with significantly higher flame speed and reaction rate. Hydrogen combustion is also subject to thermo-diffusive instabilities which are caused on account of it having lesser thermal diffusivity than mass diffusivity . This imbalance between diffusivities can cause local increase in burning rates and also local enrichment of fuel oxidizer mixture which can increase the flame speed of the flame front. It is important to study and characterize this effect to determine safe and reliable operating limits for gas turbines operating under high hydrogen content.

2.2 Boundary Layer Flashback

2.2.1 Unconfined flames

The first detailed experiments on the boundary layer flashback were performed by Lewis and von Elbe [18]. They studied methane-air flames at atmospheric and laminar conditions. They formulated a model based on the velocity gradient at the wall. Kalantari et. al extended this model to turbulent flames and derived a prediction model based on the correlations to calculate Damkohler number [13][11][12]. PSI [20] also developed a model which predicts the flashback limits. The illustration of the model based on critical velocity gradient in given below.

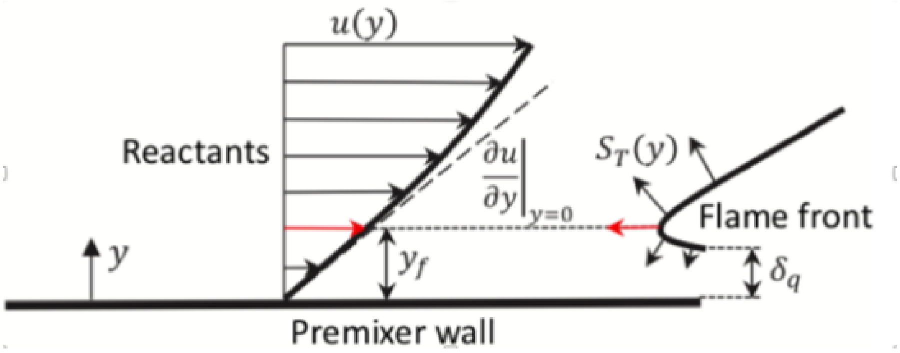

Figure 2.1: Critical velocity gradient model [11].

2.2.2 Confined flames

Although the above mentioned models describe the flashback qualitatively well, they ignore the flow - flame interaction. This interaction is generally negligent in unconfined flames and becomes relevant in confined flames. Unconfined flames can be characterized by the flame anchoring due to sudden expansion in the flow area or flame anchoring outside the burner tube. However, due to its unsteady nature, flame can creep into the burner tube or the premixer section and anchor in that section. In this region, flow - flame interaction becomes increasingly relevant and critical velocity gradient model fails to describe the flame flashback. It was found in subsequently described studies that the confined flame is more prone to flashback than the unconfined flames and thus can be used as a better control limit for flashback in gas turbines [6].

Eichler [6] studied the hydrogen flame flashback in confined flame configurations both numerically and experimentally. He found that there is an increased flashback propensity in the confined flames when compared with the unconfined flames. The description of

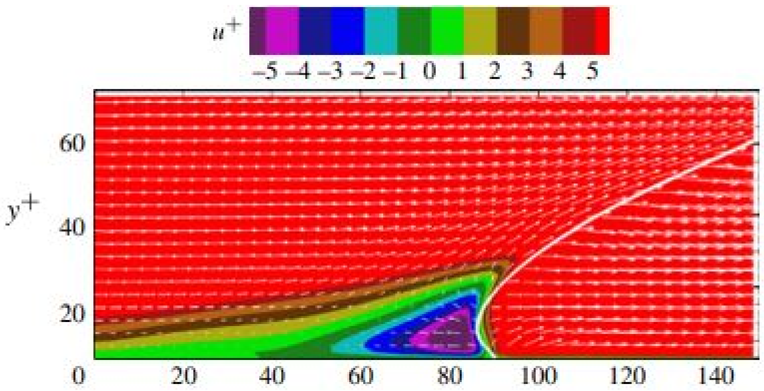

Figure 2.2: Boundary layer flashback in confined geometries. The flame front is described by the white line. As the flow approaches the flame, the streamlines curve due to the adverse pressure gradient in front of the flame front. If the flow velocity is low enough, there will be a separation in front of the flame and hence flashback. Source : Gruber[10].

boundary layer flashback phenomenon in confined flames is given in figure 2.2.

The flow expands after passing the flame due to high temperature. This causes curvature in the streamlines in incoming flow and hence generates a back pressure at the flame front. The degree of curvature is depends on the strength of the expansion and hence on the fuel-air ratio. This back pressure of the flame causes the flow to separate at the upstream of flame front. The flashback is determined by the size of separation zone and quenching distance. If size of the separation zone exceeds quenching distance, flame flows upstream and hence confined flashback occurs. This mechanism of flashback is also confirmed by LES studies of the straight channel used in Eichler experiments by Endres and Sattelmayer [7][8].

Eichler[6] performed experiments in a straight channel, 2 and 4 degree asymmetric diffusers. This allowed him to characterize the flashback phenomenon at different underlying adverse pressure gradients. He found that the mean adverse pressure gradient caused increased propensity in the flame flashback. Eichler reasoned this might be because of the increased frequencies of the low speed streaks which increase the tendency of the flame to creep upstream as seen in figure 2.3. However, this is still an open question since he reasoned there might be a hysterisis effect that might cause this.

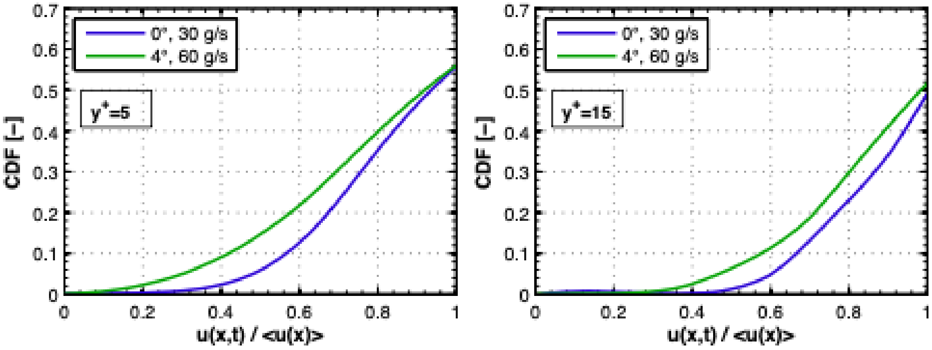

Figure 2.3: CDF of instantaneous velocity normalized by mean velocity. Results from Eichler[6].

Gruber et.al [10] performed DNS study on upward propagating Hydrogen - Air flame. In the study they observed that the low speed streaks causes the flame to bulge towards the reactants side due to the upward propagation of flame in this region. Conversely, the high speed streaks cause the downstream propagation of the flame front in this region. They also observed the existence of reverse flow regions in areas where the flame is curved towards the reactants or in the areas of low speed streaks. They reasoned this might be caused due to Darrieus Landau instability. The effect of premixed flames on turbulent flows and in particular the effect of DL instability on the existing flow is given by Lipatnikov [21] and is described in figure 2.4.

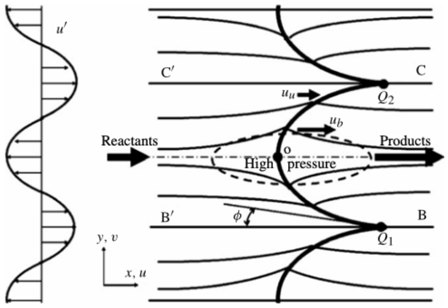

Figure 2.4: Darrieus Landau Instability as described by Lipatnikov [21].

The initial bulging of flame towards the reactants are caused by the passing of low speed streak (or ejection) across the flame front. Due to the geometry of the deformed flame front, the streamline curvature causes the development of high pressure region in front of the flame front. This high pressure region further retards the incoming fluid flow and hence further enhances the wrinkling of the flame and has positive feedback effect on this instability process. In unbounded flow, as in studies by Lipatnikov [21],the incoming fluid is retarded whereas in the wall bounded flow, due to the presence of already slow velocity, there will be a reverse flow region. The illustration of this instability is given in figure 2.4.

2.3 Premixed Flames

Combustion is said to be premixed if fuel-air mixture is homogeneous and perfectly mixed prior to combustion. Lean premixed mixtures are of particular interest since excess air reduces the temperature of the flame and hence impedes NO_x emissions. In this is section basics of laminar and turbulent premixed flames are detailed.

2.3.1 Laminar Premixed flames

Figure 2.5 shows the structure of a premixed flame. This structure is based on the solution of one dimensional, steady and adiabatic conservation equations by assuming one step reaction with large activation energy [28]. Based on figure 2.5, we can identify three main regions :

- **Unburnt side** : The mixture propagates right at laminar flame speed S_L. The mixture is characterized by equivalence ratio ϕ, unburnt temperature T_u and unburnt pressure P_u.
- **Preheat zone or Diffusion zone** : This is a chemical inert zone where transport of heat and mass occur. Heat is transported from the flame front into the unburnt

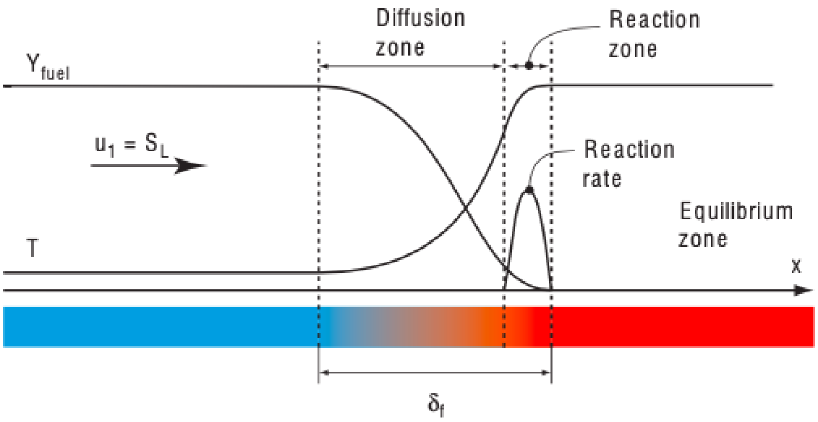

Figure 2.5: Structure of Premix flame. The flame is assumed to be stationary with fuel air mixture moving right at flame speed S$_L$.

gases and reactants are transported into the flame front from the unburnt mixture. The temperature of the mixture T starts increasing due to diffusion of heat from the flame front. Consequently, the fuel mass fraction Y$_{fuel}$ starts decreasing due to the diffusion of fuel into the reaction zone.

- **Reaction zone**: In this region, fuel is consumed and majority of the energy production takes place which can be seen by the peak in reaction rate. Combustion reactions occur and cause increase in temperature and formation of burnt products. The thickness of this zone is in general two orders of magnitude lower than the preheat zone.

In most of the flames, the preheat zone is characterized by Lewis number. It characterizes relative strength of thermal diffusion and mass diffusion in the given premixed flame. The Lewis number of the ith species in the mixture is given by,

$$Le_i = \frac{\alpha_{mix}}{D_{i,mix}} \tag{2.1}$$

Here, α_{mix} is the thermal diffusivity of the mixture and D$_{i,mix}$ is the species diffusivity of the ith species in the mixture.

Flame thickness is the combined thickness of preheat and reaction zones. Since the reaction zone thickness is two orders of magnitude lower than the preheat zone, flame thickness is considered to be equal to the thickness of preheat zone. The thickness of the preheat zone can be approximated by thermal diffusivity α_{mix} and laminar flame speed $\mathrm{S}_{l,0}$ as given below.

$$\delta_f = \frac{\alpha_{mix}}{S_{l,0}} \tag{2.2}$$

There are wide variety of numerical tools that calculate the above mentioned properties. In our current study, we use Cantera [9] to obtain flame properties.

2.3.2 Turbulent Premixed Flames

While studying the effects of turbulence on flame, it is generally assumed that turbulent flame consists of a collection of stretched laminar flamelets with a very thin reaction zone. This physical model is called the **laminar flamelet model**.

Turbulent flames are studied by comparing scales of turbulence and flame. Peters [27] identified different combustion regimes based on the relative comparison of the scales.

The turbulent velocity scale is characterized by its RMS velocity u' or turbulent kinetic energy k if isotropy is assumed. Length scale of turbulence varies from integral length scale l_t, which is the length of highest energy eddies, to kolmogorov scale η_k, which is the length of smallest eddies. In general, the isotropy assumption holds true for kolmogorov scale. Similarly, the velocity scale of the flame is given by lminar flame speed $\mathrm{S}_{l,0}$ and length scale is given by flame thickness δ_f The respective time scales are given by :

$$t_t = \frac{l_t}{u'} \tag{2.3}$$

$$t_k = \frac{\eta_k}{u'(\eta_k)} \tag{2.4}$$

$$t_c = \frac{\delta_f}{S_{l,0}} \tag{2.5}$$

Here, the subscripts t,k and c refer to integral scale, kolmogorov scale and chemical scale respectively.

Based on the relative strengths of these time scales, we have two dimensionless numbers that compare the turbulent scale to flame scale. Damkohler number compares integral scale to the flame scale and is given by :

$$Da = \frac{t_t}{t_c} = \frac{l_t S_{l,0}}{u' \delta_f} \tag{2.6}$$

Karlovitz number compares kolmogorov scale to flame scale and is given by ;

$$Ka = \frac{t_k}{t_c} = \frac{u'(\eta_k)\delta_f}{\eta_k S_{l,0}} = \left(\frac{l_t}{\delta_f}\right)^{-0.5} \left(\frac{u'}{S_{l,0}}\right)^{1.5} \tag{2.7}$$

Consequently, the turbulent reynolds number is given by,

$$Re_t = \frac{u' l_t}{S_L \delta_f} \tag{2.8}$$

Based on the dimensionless numbers mentioned above, Peters [27] gave combustion regimes diagram shown in figure 2.6.

The different regimes in the diagram are explained as follows :

- **Laminar flames :** The combustion is laminar.
- **Wrinkled flames :** The turbulence in the base flow causes wrinkling in the flame front resulting in larger area and thus increase in the burning intensity of the flame.
- **Corrugated flames :** The velocity scale of turbulence is higher than the velocity scale of the flame. Thus the wrinkling is more significant than the wrinkled flames leading much higher flame surface area and burning intensities. However the flame thickness (preheat zone and reaction zone) is still smaller than the length scale of turbulence. Although the flame is wrinkled by the incoming turbulence, there is no effect on the internal structure.

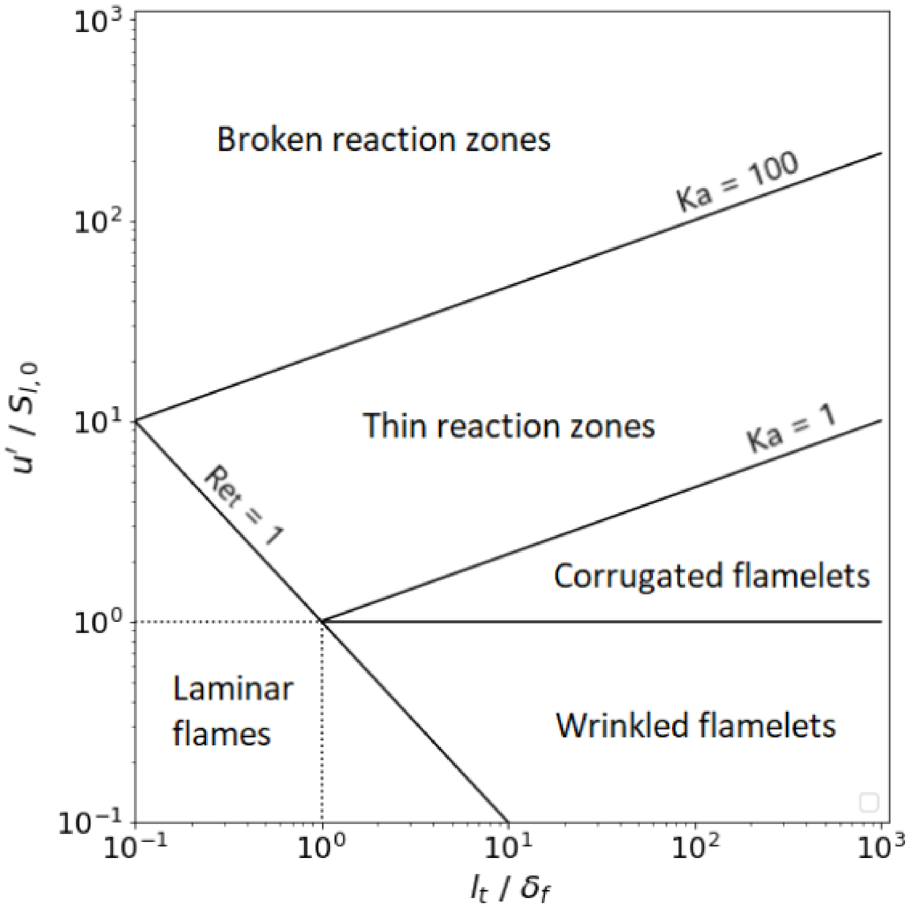

Figure 2.6: Combustion regimes according to Peters[27]. Figures from Poinsot[28].

- **Thin reaction zone :** The kolmogorov eddies penetrate the flame and enhance mixing in the preheat zone which causes the preheat zone to become thicker. Heat and mass diffusion are also affected by turbulent eddies. The reaction zone is still not perturbed by turbulent eddies.

- **Broken reaction zone :** The kolmogorov eddies penetrate into the reaction zone and can cause change in the internal structure of reactive layer. Laminar flamelet theory is not valid anymore in this regime.

2.3.3 Influence of flowfield on premixed flame

The presence of non uniform and unsteady flowfield can have significant influence on the dynamics of premixed flames. A good overview of these interactions is given by C.K.Law and Sung [15].

The effect of non uniform base flow field on the premixed flame is called stretch.The influence of stretch on the flame is generally characterized by stretch rate κ given below.

$$\kappa = \frac{1}{A}\frac{DA}{Dt} \tag{2.9}$$

where, $\frac{D}{Dt}$ represents the material derivative operation and A is the area of the flame surface element. This stretch rate can be further developed to yield :

$$\kappa = \nabla_t.\mathbf{u} + (\mathbf{S}_f.\mathbf{n})(\nabla.\mathbf{n}). \tag{2.10}$$

Here, ∇_t is tangential gradient operator, $\mathbf{u}$ is the velocity of the underlying base flow, $\mathbf{S}_f$ is the velocity of the flame surface and $\mathbf{n}$ is the normal vector of the flame surface element. The first term in the equation incorporates effects due to non uniform velocity (strain) and second term incorporates the effects due to curvature. Different types of stretched flames are given in figure 2.7.

Flame stretch effects are more prevalent to non equidiffusive mixtures (Le $\neq 1$). The non conservative nature of flame response due to uneven heat and mass diffusivities can lead to local rise or fall in burning intensities of the flame. Figure 2.8 below shows the effect of nonequidiffusion on stretched flames.

The top part of the figure illustrates a planar flame in strained flow field. Note that both heat and mass diffusion occur normal to the flame surface. In case of mixtures with Le < 1, mass diffusion is greater than the heat diffusion. The flame surface losses energy to the incoming streamlines by heat diffusion and gains energy from the streamlines by species diffusion. In Le < 1 flames, the energy gain due to mass diffusion is greater than the loss due to heat diffusion and hence the burning intensity of the flame is increased. Converse is true for Le > 1 flames.

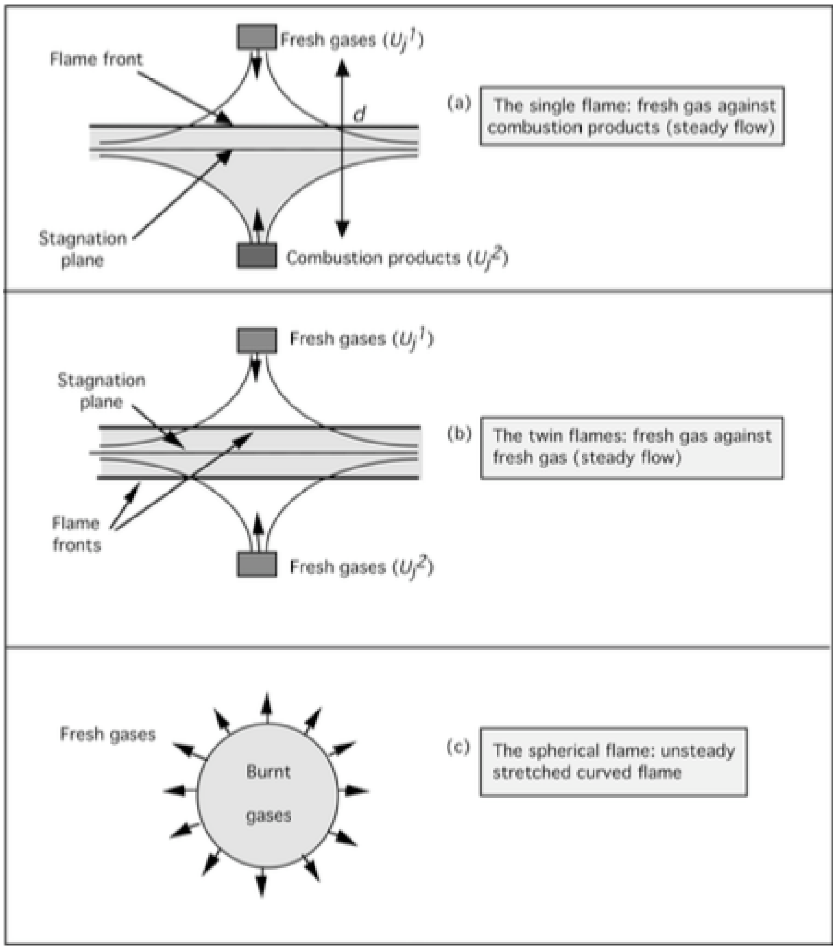

Figure 2.7: Stretched flames due to curvature and flow strain. In the first two figures, the flow is strained and the flame is planar. In the third figure, there are no straining effects and flame behaviour is modified only due to curvature of the flame front [28].

The bottom part of the figure illustrates a bunsen burner flame. Notice that flame is curved at the tip. Considering this part of the flame, heat diffusion plays a focusing effect wherein heat loss from the flame front heats up the incoming flow. Conversely, mass diffusion plays a defocusing effect such that the reactant concentration of the incoming flow is reduced. In Le < 1 flames, the focusing effect of the heat diffusion is less than the defocusing effect of mass diffusion. Hence, the burning intensity of the flame is reduced. This is the tip opening effect prevalent to hydrogen bunsen flames. Converse is true for Le

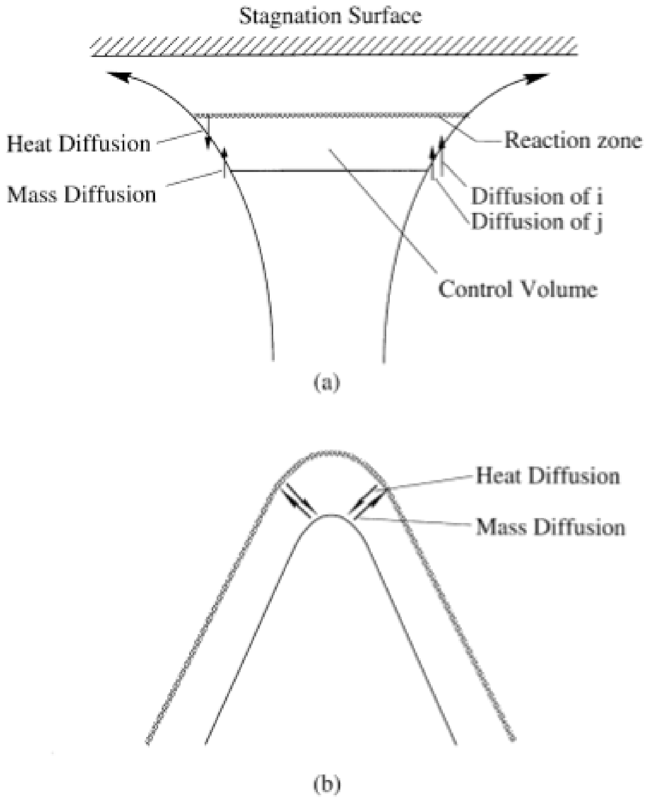

Figure 2.8: Non equidiffusion effects on stretched flame. Top part of the figure displays typical stagnation flame where flamefront is planar. Bottom part of the figure displays bunsen burner flames [15].

> 1 flames.

With respect to stretch, the stretched flame speed is dependent on stretch rate, laminar flame speed and Lewis number of the fuel air mixture. However, the stretched laminar flame speed is conviniently expressed as given by Markstein [22] :

$$S_{l,s} = S_{l,0} - L_M \kappa \tag{2.11}$$

Here, L$_M$ is called as Markstein length of unburnt mixtures which is determined from experimental and numerical studies.This relation generally holds well for weakly stretched flames and flames with Le close to 1.

2.3.4 Instabilities

Most of the discussion upto this point assumed premixed flames studied to be stable. However instabilities can occur in the flame and can lead to formation of cellular structure and ridges in the flame as can be seen in figure 2.9.

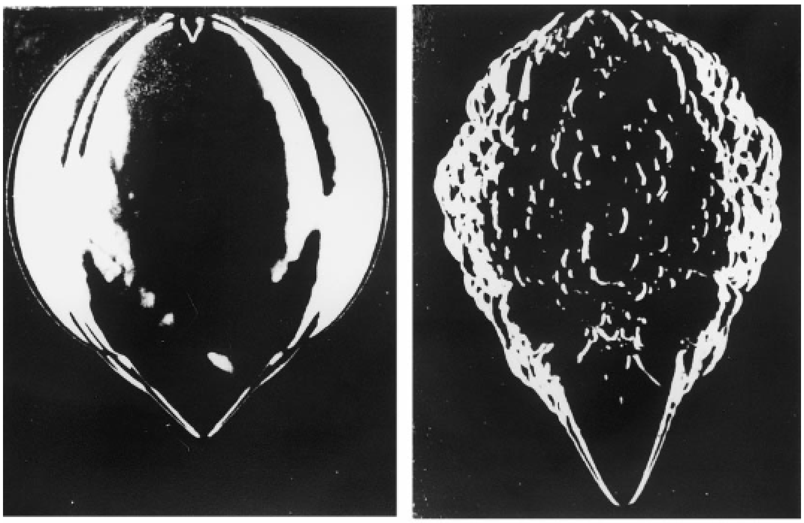

Figure 2.9: Cellular instabilities. The left part of the figure shows butane flame which is cellularly stable. The right part of the figure shows hydrogen flame which is cellularly unstable [15].

Hydrodynamic Instability

Assume a planar flame front perturbed by underlying flow field as shown in figure 2.10. Assuming the flame thickness to be much smaller than the perturbation scale, we can see segments of the flame that are convex and concave towards the reactants. Due to thermal expansion effects of the flame, the convex segments cause an increase in the area of incoming streamtube. This causes the incoming flow to slow down and thus formation of a higher pressure region upstream of the convex segment. The converse is true for concave segments where flow accelerates and forms a low pressure region. The low velocity region further causes the convex region to move upstream and further increase the stream tube

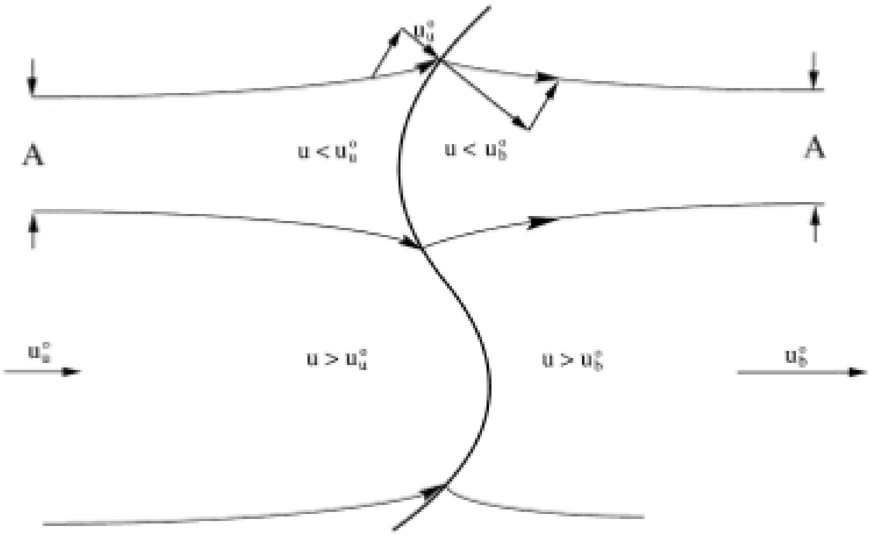

Figure 2.10: Hydrodynamic instability. Sections that are convex towards the reactants cause decelaration in the incoming flow due to streamtube expansion. Conversely, concave sections cause streamtube contraction and thus acceleration of the flow [15].

area. This instability is also referred to as Darrieus Landau (DL) instability. Since we did not make any considerations on the perturbation wavelength, the flame front is unstable to all perturbation wavelengths for this instability.

Thermo-diffusive instabilities

These instabilities occur due to non equal strengths of thermal and mass diffusion. Assuming the same convex-concave flame segment and Le < 1, the burning is intensified in the convex segments due to higher transport of species and causes the surface to move upstream due to higher laminar flame speed. In concave segments, the reactants are dispersed due to the concave segments and cause lower burning intensity and flame speed. The converse is true for Le > 1 flames. The schematic of thermo-diffusive instabilities are given in figure 2.11.

It has been found in numerical solutions that hydrodynamic instability generates regular cells whereas cells generated due to thermo-diffusive instabilities are chaotic in nature [15].

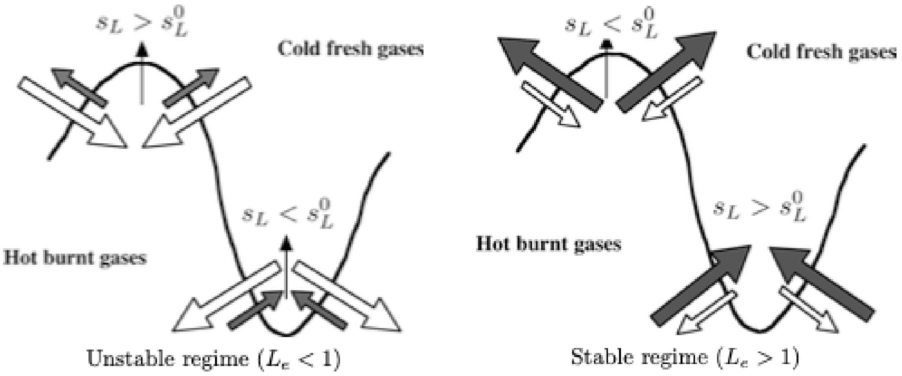

Figure 2.11: Thermo-diffusive Instabilities. Left part of the figure shows flame characterized by Le < 1. Right part of the figure shows a flame characterized by Le > 1 [28].

2.3.5 Darrieus Landau (DL) Instability

Assuming the the flame front to be infinitely thin ($\delta_l = 0$), the dispersion relation for the growth rate of DL instability is given by Matalon [23] as :

$$\sigma_{DL} = \Gamma(\varphi) S_L k. \tag{2.12}$$

where, σ_{DL} is the DL instability growth rate, S_L is the laminar flame speed of the fuel-oxidant mixture and k is the perturbation wave number. Γ is given by :

$$\Gamma(\varphi) = \frac{\varphi}{\varphi + 1}\left[\sqrt{\varphi + 1 - \varphi^{-1}} - 1\right] \tag{2.13}$$

where, φ is ratio of unburnt gas density to burnt gas density.

Bychukov et. al [3] gave the dispersion relation assuming small but finite flame thickness and also considering thermal conduction stabilisation of small scale perturbations. The dispersion relation after taking these considerations is given by :

$$\sigma_{DL} = \Gamma S_L k \left(1 - k/k_c\right) \tag{2.14}$$

where, k_c is the cut-off wave number related to thermal stabilisation. Small scale perturbations with $k > k_c$ are suppressed due to thermal conduction. Large scale perturbations with k < k_c grow exponentially.

The cut-off wavelength, λ_c is given by :

$$\lambda_c = \delta_L \frac{\pi(\varphi - 1)}{\Gamma\sqrt{\varphi + 1 - \varphi^{-1}}} \left(1 + \varphi \ln \varphi \left[\frac{\varphi + 1 + 2}{(\varphi - 1)^2}\right]\right) \tag{2.15}$$

In strong turbulence, coherent turbulent structures can prevent DL instability to develop. Chaudari et.al [4] proposed that the instability can grow in the presence of external turbulence if the characteristic instability growth rate is larger than the turbulent coherent structure frequency. Hence, DL instability is sustained in turbulence if :

$$\sigma_{DL} > \omega_{turb} \tag{2.16}$$

where, ω_{turb} is the turbulent frequency. It should be noted that only turbulent structures that have k that is same or lower than the one used in σ_{DL} has effect this instability. Only under this assumption, the separation of time scales is valid. Wave numbers smaller than k smooth out the corrugations due to instability, but the frequency is also smaller. Structures with wave numbers larger than k can increase the corrugations at finer scales, but their amplitudes decrease with increasing wave number. Hence, statistically the most relevant wave number that can suppress the instability growth is the same wave number as the wave number used in predicting the σ_{DL}.

2.4 Turbulent Boundary Layers

2.4.1 Time mean structure

Turbulent boundary layers are characterized by different regions as shown in figure 2.12 [26]. Analytical solutions of turbulent boundary layers do not exist. However, if the relevant scaling is used, there is a self similar behaviour. In general, turbulent boundary layers contain three regions based on the distance from the wall as shown in figure 2.12 .

Friction velocity is given by :

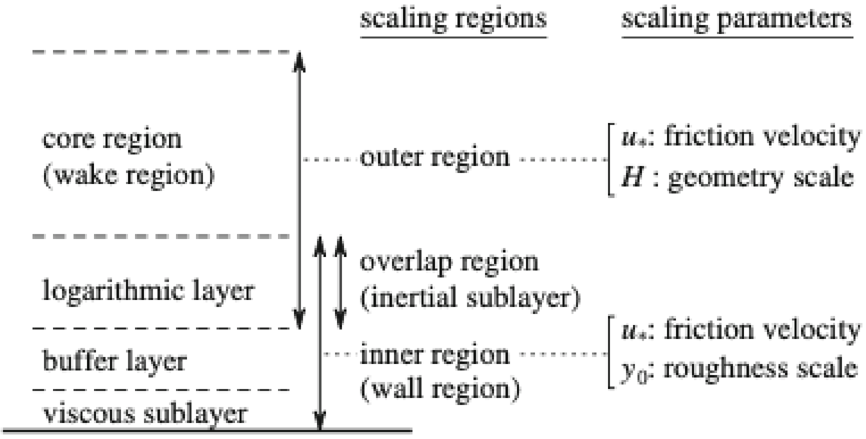

Figure 2.12: Scaling regions [26]

.

$$u_\tau = \sqrt{\frac{\tau}{\rho}}. \tag{2.17}$$

Here τ is the wall shear stress and ρ is the density of the fluid.

In the outer region, turbulent shear is dominating. Velocity scales with friction velocity u_τ and length scales with the flow geometry scale H. The scaling law, also called as **velocity-defect law** is given by :

$$\frac{u_o - \bar{u}}{u_\tau} = F\left(\frac{y}{H}\right). \tag{2.18}$$

In the inner region, viscous forces are dominating. Here, the velocity scales with friction velocity u_τ and length scales with the inner scale y^+. The y^+ is given by :

$$y^+ = \frac{y u_\tau}{\nu}. \tag{2.19}$$

where, y is the distance from the wall. The following scaling law holds for the inner layer:

$$\frac{\bar{u}}{u_\tau} = f\left(y^+\right) \tag{2.20}$$

In general, the inner region contains the viscous sub layer($y^+ < 5$) and the buffer layer($5 < y^+ < 30$). In the viscous sublayer, velocity scales linearly with wall distance and in the buffer layer most of the turbulent energy production and the maximum in the turbulent stresses occur.

The scaling law for the overlap layer is obtained by equating the velocity profile gradients at the boundaries of inner and outer regions. This yields the very familiar logarithmic layer given by :

$$\frac{\bar{u}}{u_\tau} = \frac{1}{k}\ln y^+ + 5.0 \tag{2.21}$$

Here, k is called as von Karman constant and takes the value 0.41 .

If mean velocity is scaled with inner variables, the velocity profiles in the inner and overlap region take a canonical form fitted by empirical functions. One such function is Spalding profile [34] which we will use in this work. The spalding profile is given by :

$$y^+ = u^+ + e^{-5k}\left[e^{ku^+} - 1 - ku^+ - \frac{(ku^+)^2}{2} - \frac{(ku^+)^3}{6}\right]. \tag{2.22}$$

The turbulent stresses depend on the Reynolds number of the flow. Moser et.al [24] performed DNS of a turbulent channel flow at three different reynolds numbers. The Reynolds number used by them i thes friction Reynolds number given by :

$$Re_\tau = \frac{u_\tau \delta}{\nu}. \tag{2.23}$$

Here, δ is the channel half height. The Reynolds numbers they investigated are 180, 395 and 590. The distribution of the turbulent stresses are given below in figure 2.13. The peak value of the stresses and the location of peak are in general function of reynolds number.

2.4.2 Time resolved structure

Studies in turbulent boundary layers showed existence of large scale coherent structures. A good overview of these structures is given by Robinson [30].The quadrant analysis given

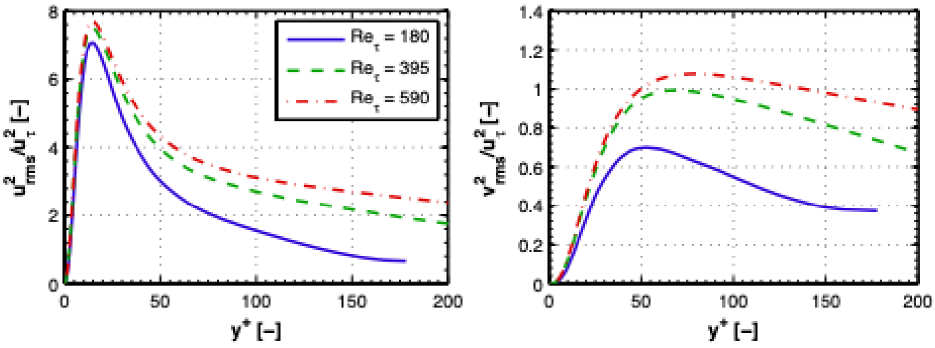

(a) Normal stress in x-direction.

(b) Normal stress in y-direction.

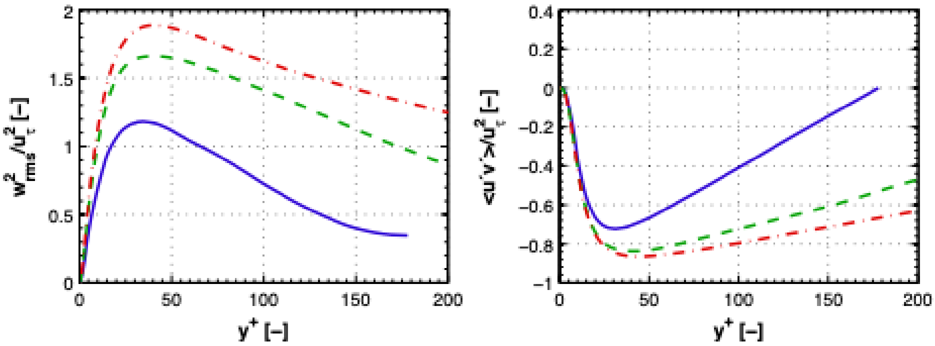

(c) Normal stress in z-direction.

(d) Reynolds stress $\langle u' v' \rangle$.

Figure 2.13: Moser results [24]

.

by Wallace [36] is used to identify the structures. These structures are classified according to the sign of streamwise and wall-normal fluctuations as given in figure 2.14.

Events which yield the product u'v' as negative (and thus positive turbulent energy production) are characteristic flow events. These events are Q2 events, which are called as ejections and Q4 events, which are called as sweeps. The other events are interactions betweeen the two characteristic events.

Some of the details of these structures in low reynolds number flow that are of consensus in the community are given below :

1. Viscous layer, despite being associated with being laminar, is not laminar at all. It consists of elongated regions of low and high speed fluid (with respect to mean velocity at the location) with lengths of the order of 1000 L^+ and with average spacings of

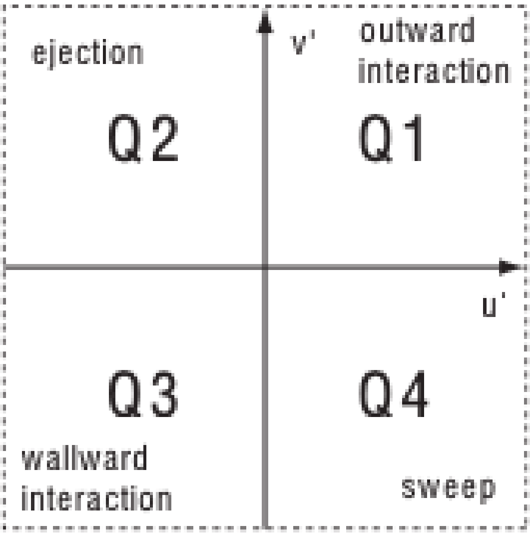

Figure 2.14: Quadrant decomposition by Wallace [36]. Figures obtained from [6]

.

100 L^+. Here, L^+ is the viscous length scale given by:

$$L^+ = u_\tau/\nu. \tag{2.24}$$

2. Low speed streaks are associated with quasi streamwise vortices that have diameter of 30 L^+ [29]. Since these vortices are generally smaller than the streaks, it is thought that these vortices generally drag the streaks in the near wall and they convect downstream.

3. The buffer layer is characterized by Q2 events. These processes are responsible for most of the turbulent energy production in the buffer layer. Q2 events dominate above the buffer layer, whereas sweep events dominate in the near wall regions.

4. Existence of hairpin, horseshoe and λ shaped vortices that influence the dynamics of turbulence production.

2.5 Influence of adverse pressure gradient on turbulent boundary layers

2.5.1 Time mean structure

Equation 2.18 gives us the scaling law for the outer region. However, this is only true for cases where there is no pressure gradient. Assuming most of the influence in the inner region comes from shear stress, the influence of pressure gradient can be included by a dimensionless parameter given by :

$$\beta = \frac{\delta^*}{\tau}\frac{dp}{dx}. \tag{2.25}$$

β is known as the Clauser parameter and δ^* is the displacement thickness. Boundary layers with constant value of β^* are called equilibrium boundary layers [26]. The scaling law is now generalized to:

$$\frac{\bar{u} - u_o}{u_\tau} = F\left(\frac{y}{H}, \beta\right) \tag{2.26}$$

Although we assume no influence of the pressure gradient in the inner and overlap region, recent studies have shown that mean velocity profile shifts below the canonical profile of the channel flow. However, this is still in discussion.

Carlos et. al [35] performed study on the turbulence statistics in the adverse pressure gradeint flows. They found that increasing pressure gradient strengthened the wake region and increased the velocity defect. They also identified a region of second peak in the turbulent stresses in the logarithmic layer as shown in figure 2.15 . This peak is caused due to low and high momentum regions in the log layer. Increasing β while keeping Re_τ constant increases peak intensity without changing location whereas changing Re_τ changed the peak location.

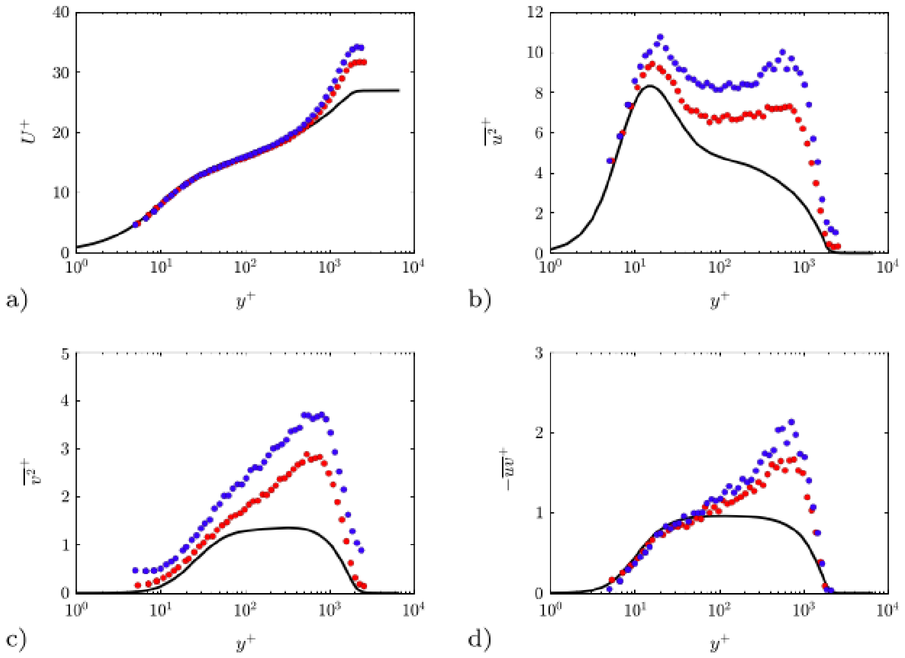

Figure 2.15: Overview of time mean structure obtained by Carlos et. al [35]. Red ($\beta = 1.3$), Blue ($\beta = 2.4$) and solid line is zero pressure gradient

.

2.5.2 Time resolved structure

Lee et.al [17] performed studies on the structures in turbulent boundary layer under adverse pressure gradient. They considered zero, moderate and strong pressure gradients and equilibrium boundary layers. They found that the streaks are shorter compared to zero pressure gradient flows as shown in figure 2.16. The spacing between the streaks has increased as well. Low speed streaks are still longer than high speed streaks. The streaks in general meander strongly compared to zero pressure gradient flow. They found that adverse pressure gradient augments the angle of inclination of packets and spacing of the vortex. This led to reduction in Q2 events. Although Q2 events are found to be dominating structures in zero pressure gradient flows, there is an increasing influence of Q4 events in the adverse pressure gradient flows. They concluded that the near wall streaks are weakened by adverse pressure gradient and outer structures are augmented.

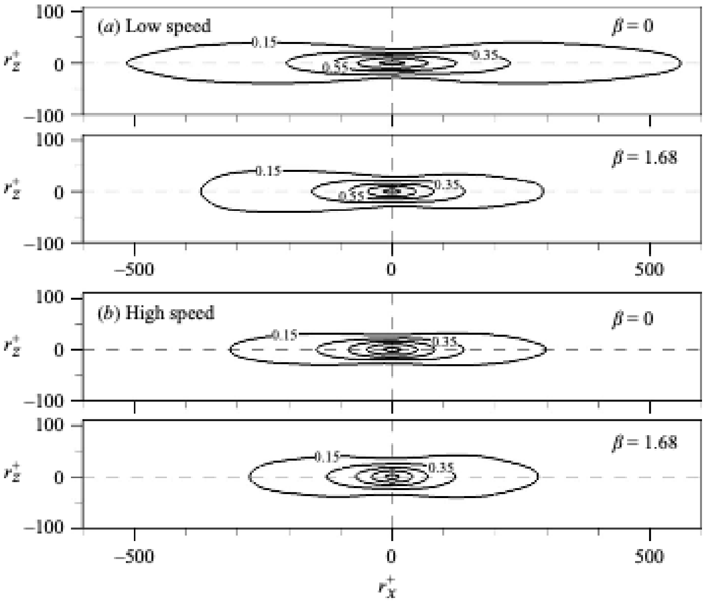

Figure 2.16: Conditional correlations of streaks. All the dimensions are normalized by viscous units. Starting from 0.15, contour levels increase by 0.2. Figures from [17]

.

Recent studies by Bross et.al [2] involved studying interaction between structures in near wall region and log layer in the adverse pressure gradient flow. They particularly focused on the influence of these structures in reverse flow events. In general, the low and high momentum regions in the log layer cause the appearance of the second peak in the turbulent stresses. They concluded existence of low speed streaks is necessary condition for reverse flow event to occur. They gave a conceptual model as illustrated in figure 2.17. They noted following observations :

1. Low speed streaks near wall must be strongly decelerated by the low momentum region in the log layer.
2. Due to the meandering of low speed streaks, the streamwise vortex filaments get tilted with respect to flow direction and can cause reverse flow events.
3. Spanwise vortices located near the wall and low speed streaks also cause strong reverse flow events.

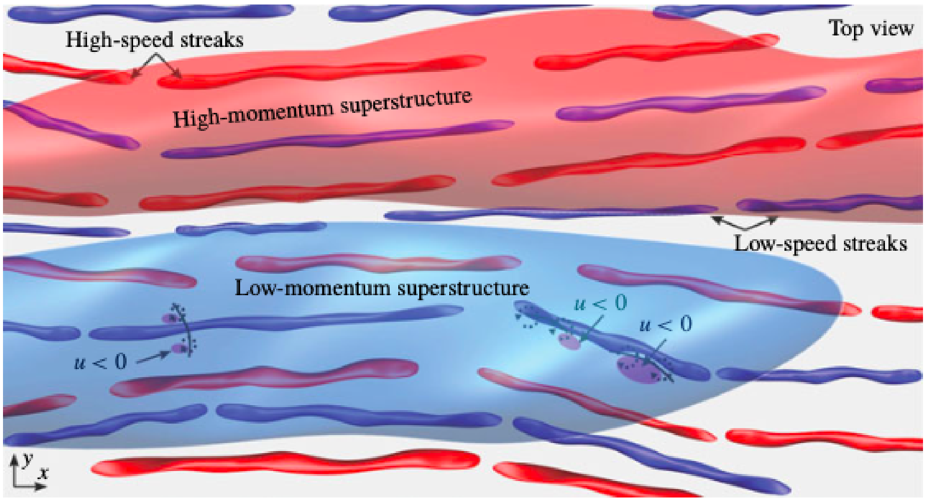

Figure 2.17: Conceptual model showing the interaction between structures that can cause a reverse flow event [2]

.

So far the discussion in adverse pressure gradient flows is limited to external flows. There might be different dynamics that dictate the physics in internal flows. Internal adverse pressure gradient flows are achieved in diffusers with increasing flow area.

Lee et.al [16] performed DNS studies in a conical diffuser with varying opening angles. Increasing opening angle increases the adverse pressure gradient in the flow. The flow in these diffusers is characterized as non equilibrium adverse pressure gradient flow. Hence, there is no self similarity observed in mean velocity profiles. The wake strength is also higher due to the combined effects of the presence of upper wall and the adverse pressure gradient. An outer peak in turbulence intensities similar to free adverse pressure gradient flows is observed. The streaks in the near wall region are also shortened. However, contrary to the observations in the free adverse pressure gradient flow, the outer streaks have increased streamwise extents. This is due to merging of streaks due to reducing bulk velocities due to expansion. Q4 events became much more dominant compared to straight pipe.

2.6 Research question

In this thesis LES simulations are carried out for channel and 2 degree diffuser geometries studied by Eichler. It aims to elucidate the details of the changes in the turbulent structures due to APG and how they might affect the flashback propensity. First, detailed study of the turbulent structures in the near wall region is performed. Then, an attempt at the effects these changes have on the flame propagation and specifically DL instability is studied.

Chapter 3

Numerical Modeling

The governing equations of fluid flow are based on the conservation laws of physics, namely:

- Mass of a system is conserved.
- Momentum of a system is conserved.
- Energy of a system is conserved.

The fluid is generally regarded as a continuous medium. Since most of the analysis occurs at macroscopic scales (greater than 1μm), the molecular structure and motions are ignored.

Applying mass and force balances to the fluid control volume, we obtain Navier-Stokes equations. Assuming the flow is incompressible, the density of the fluid becomes constant and the equations are further simplified into the vector form :

$$\nabla.\mathbf{u} = 0 \tag{3.1}$$

$$\frac{\partial \mathbf{u}}{\partial t} + (\mathbf{u}.\nabla)\,\mathbf{u} = -\frac{1}{\rho}\nabla p + \nu\nabla^2\mathbf{u} + S_u \tag{3.2}$$

Here, ρ is the density, $\mathbf{u}$ is the velocity, p is the pressure, S_u is the momentum source term, ∇ is the gradient operator and ν is the kinematic viscosity. ∇^2 is the Laplacian operator given by:

$$\nabla^2 = \nabla.\nabla \tag{3.3}$$

Kinematic viscosity is obtained from dynamic viscosity by:

$$\nu = \frac{\mu}{\rho} \tag{3.4}$$

In order for these equations to hold, the fluid must be incompressible, Newtonian and viscous without any sources of fluid.

The Navier-Stokes equations in the Einstein notation are given by :

$$\frac{\partial u_i}{\partial t} + u_j \frac{\partial u_i}{\partial x_j} = -\frac{1}{\rho}\frac{\partial p}{\partial x_i} + \nu \frac{\partial^2 u_i}{\partial x_j \partial x_j} \tag{3.5}$$

$$\frac{\partial u_i}{\partial x_i} = 0 \tag{3.6}$$

where, u_i is the ith component of velocity.

The first term on the left side of the equation is the local time rate of change of the velocity and the second term represents the advection of velocity. The first term on the right side is the pressure gradient that drives the flow and the second term is the description of viscous diffusion. The last term is the source term that can include surface tension forces or the gravity.

3.1 Reynolds Averaged Navier -Stokes equations

In order to solve the Navier-stokes equations, the computational domain must be resolved down to the Kolmogorov scales. This increases computational costs and also limits the application to a very few simple cases. A more practical way is to solve the Reynolds averaged Navier-Stokes (RANS) equations instead. The idea behind the RANS is to obtain time averaged quantities instead of the instantaneous quantities.

The instantaneous quantities are decomposed into mean and fluctuating quantities as follows:

$$\mathbf{u} = \overline{\mathbf{u}} + \mathbf{u}' \tag{3.7}$$

$$p = \overline{p} + p' \tag{3.8}$$

where, the operator $^{-}$ denotes time averaging and $'$ denotes fluctuation from the mean value. Some algebraic properties of the averaging operation are given below:

$$\overline{a'} = 0 \tag{3.9}$$

$$\overline{a\overline{b}} = \overline{a}\overline{b} \tag{3.10}$$

$$\overline{a'b'} \neq 0 \tag{3.11}$$

Substituting the decompositions (3.7) and (3.8) in the Navier-Stokes equations and using the properties (3.9), (3.10) and (3.11), we obtain RANS equations as follows :

$$\frac{\partial \overline{u_i}}{\partial x_i} = 0 \tag{3.12}$$

$$\frac{\partial \overline{u_i}}{\partial t} + u_j \frac{\partial \overline{u_i}}{\partial x_j} = \frac{1}{\rho}\frac{\partial \overline{p}}{\partial x_i} + \nu \frac{\partial^2 \overline{u_i}}{\partial {x_j}^2} - \frac{\partial \overline{{u_i}'{u_j}'}}{\partial x_j} \tag{3.13}$$

As we can see in the above equations, there is a new unknown term $\overline{{u_i}'{u_j}'}$. This term is referred as the Reynolds stress and has six components (three diagonal and three off-diagonal). This term causes the closure problem for solving the equations and has to be modeled. The most common way of modeling this term is by using eddy viscosity hypothesis. Under this model, the reynolds stress is given by ;

$$-\overline{{u_i}'{u_j}'} = \nu_t \left(\frac{\partial \overline{u_i}}{\partial x_j} + \frac{\partial \overline{u_j}}{\partial x_i} \right) - \frac{2}{3} k \delta_{ij} \tag{3.14}$$

where, ν_t is the turbulent viscosity, k = $\frac{\overline{{u_i}'{u_i}'}}{2}$ is the turbulent kinetic energy. The turbulent viscosity ν_t is generally estimated by using different turbulence models.

3.2 Large Eddy Simulation

Although RANS models are easy to use, there is no general purpose model that is widely applicable to practical applications. This can be due to the differences in the large scale and small scale eddies. The small scale eddies are in general isotropic and have an universal behaviour. The large scale eddies on the other hand are highly anisotropic and their behaviour depends on the geometry of the domain and the boundary conditions. Large Eddy Simulation (LES) models the small scale eddies using the universally observed behaviour and computes the larger scale eddies directly.

3.2.1 Filtered Navier Stokes equations

LES uses a spatial filtering operation to resolve large eddies. The filtering operation is given by :

$$\widetilde{\phi(\mathbf{x{,}t})} = \iiint\limits_V G(\mathbf{x}, \mathbf{x}', \Delta)\phi(\mathbf{x}', t)d\mathbf{x}' \tag{3.15}$$

where the over-tilde represents the filtered field, G represents the spatial filtering function and Δ is the filter cut-off length. The filter cut off length is generally taken as:

$$\Delta = (\Delta x \Delta y \Delta z)^{\frac{1}{3}} \tag{3.16}$$

where Δx, Δy and Δz are the grid spacings in x, y and z directions respectively. The filtering function used in the current work is the top-hat filter given by :

$$G(\mathbf{x}, \mathbf{x}', \Delta) = \begin{cases} \frac{1}{\Delta^3} & |\mathbf{x} - \mathbf{x}'| \leq \Delta/2 \\ 0 & otherwise \end{cases} \tag{3.17}$$

Performing the filtering operation on the Navier-Stokes equations, we obtain :

$$\frac{\partial \widetilde{u_i}}{\partial t} + \frac{\partial \widetilde{u_i u_j}}{\partial x_j} = -\frac{\partial \widetilde{p}}{\partial x_i} + \frac{\partial}{\partial x_j}\nu\left(\frac{\partial \widetilde{u_i}}{\partial x_j} + \frac{\partial \widetilde{u_j}}{\partial x_i}\right) \tag{3.18}$$

where $\widetilde{u_i u_j}$ is an unknown quantity. Expanding this further by :

$$\widetilde{u_i u_j} = \widetilde{u}_i \widetilde{u}_j - \frac{\tau_{sgs}}{\rho} \tag{3.19}$$

where τ_{sgs} is the subgrid stress given by :

$$\tau_{sgs} = -\rho(\widetilde{u_i u_j} - \widetilde{u}_i \widetilde{u}_j) \tag{3.20}$$

Substituting the above derivations, we obtain the filtered Navier-Stokes equations given by :

$$\frac{\partial \widetilde{u}_i}{\partial t} + \frac{\partial \widetilde{u}_i \widetilde{u}_j}{\partial x_j} = -\frac{\partial \widetilde{p}}{\partial x_i} + \frac{\partial}{\partial x_j} \nu \left(\frac{\partial \widetilde{u}_i}{\partial x_j} + \frac{\partial \widetilde{u}_j}{\partial x_i} \right) + \frac{1}{\rho} \frac{\partial \tau_{sgs}}{\partial x_j} \tag{3.21}$$

$$\frac{\partial \widetilde{u}_i}{\partial x_i} = 0 \tag{3.22}$$

The effect of the smaller eddies on the larger scales is incorporated by the term τ_{sgs}. As we can see, there is a closure problem due to this term. Eddy-viscosity can be used to model these terms since the assumptions underlying it are true for microstructure. Similar to RANS counter part, the subgrid stress is given by :

$$\tau_{sgs} = \nu_{sgs} \left(\frac{\partial \widetilde{u}_i}{\partial x_j} + \frac{\partial \widetilde{u}_j}{\partial x_i} \right) \tag{3.23}$$

where ν_{sgs} is subgrid eddy viscosity. Different models exist to describe the subgrid eddy viscosity. The models used in the current work are Smagorinsky model and wall-adapting local eddy-viscosity (WALE) model.

3.2.2 Smagorinsky Model

The Smagorinsky model [33] uses the Boussinesq assumption since the smallest eddies are isotropic. It was originally proposed for use in meteorological applications. Due to this, less emphasis is based on wall boundaries. This model assumes local equilibrium between the production and dissipation of subgrid turbulent kinetic energy. The subgrid turbulent viscosity is defined as :

$$\nu_{sgs} = {L_s}^2 \left(2\overline{S_{ij}}\;\overline{S_{ij}}\right)^{1/2} \tag{3.24}$$

where, $L_s = C_s\Delta$ is Smagorinsky length scale and $\overline{S_{ij}}$ is the filtered strain rate tensor given by:

$$\overline{S_{ij}} = \frac{1}{2}\left(\frac{\partial \widetilde{u_i}}{\partial x_j} + \frac{\partial \widetilde{u_j}}{\partial x_i}\right) \tag{3.25}$$

Few drawback of Smagorinsky model are :

- Poor behaviour in the near wall regions since the length scale does not tend to zero at the wall.
- The Smagorinsky constant, C_s is treated as an universal constant.

The first drawback can be overcome by using Van Driest damping [19] to the filter length Δ. The damping function is given by:

$$f = 1 - e^{\frac{-y^+}{A}} \tag{3.26}$$

where y$^+$ in the wall distance in the inner scaled units. The filter length is them obtained as :

$$\Delta = min\left(\frac{\kappa y}{C_s} f, \Delta\right) \tag{3.27}$$

here, $\kappa = 0.41$, A $=$ 28, $C_s = 0.158$ and y is the wall distance.

3.2.3 WALE Model

The wall adapting local eddy viscosity (WALE) model [25] considers a more general algebraic approach. It has advantages in being computationally inexpensive due to its algebraic nature and also performs correctly in the vicinity of the walls ($\nu_{sgs} \propto y^3$). Taking the traceless symmetric part of the square of the velocity gradient tensor :

$$S_{ij}{}^{d} = \frac{1}{2}\left(\overline{g_{ij}}^2 + \overline{g_{ji}}^2\right) - \frac{1}{3}\overline{g_{kk}}^2\delta_{ij} \tag{3.28}$$

where $\overline{g_{ij}}$ is the filtered velocity gradient tensor $\frac{\partial \widetilde{u_i}}{\partial x_j}$. The subgrid viscosity ν_{sgs} is then given by:

$$\nu_{sgs} = (C_w \Delta)^2 \frac{\left(S_{ij}{}^d S_{ij}{}^d\right)^{3/2}}{\left(\overline{S_{ij}}\ \overline{S_{ij}}\right)^{5/2} + \left(S_{ij}{}^d S_{ij}{}^d\right)^{5/4}} \tag{3.29}$$

where $C_w = 0.325$ is the model constant.

Chapter 4

Zero degree Channel

4.1 Numerical setup

The computational domain of the channel is given below. The dimensions of the domain are chosen in accordance with the recommendations by Mukhza et.al. The channel must be long and wide enough for the fluctuations to be uncorrelated so that there is no overestimation of the turbulent stresses. The simulations are performed for two cases characterized by inlet bulk velocities of 10m/s and 20 m/s.

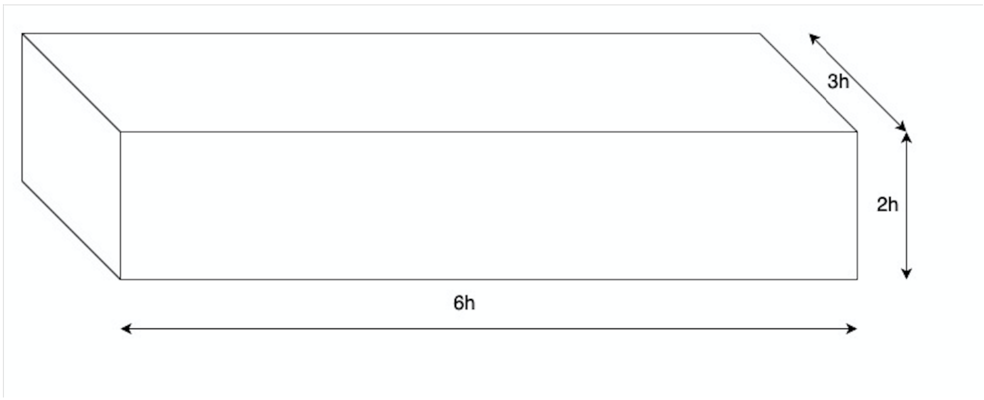

Figure 4.1: Computational domain of the channel

.

The domain is meshed uniformly along streamwise (x) and spanwise (z) directions. The cell size is increased along the wall normal direction with $y^+ = 0.6$ for the first cell adjacent to the wall normal boundaries. Approximately 5 cells are placed in the viscous sub-layer.

The simulations are performed in open source code OpenFOAMv2006. PIMPLE solver has been used which is a hybrid between SIMPLE and PISO algorithms. Time step is adjusted to keep maximum Courant number at 0.75.

The mesh and the simulation settings are given below :

Table 4.1: Simulation and mesh settings for the channel

Cases	**10m/s**	**20m/s**
Cells	1.5 million	9 million
Wall y^+	0.6	0.6
Δx^+	13	13
Δz^+	9	9
Solution method	PIMPLE	PIMPLE
SGS model	Smagorinsky,WALE	WALE

4.1.1 Initial and boundary conditions

In order to obtain statistically homogeneous and fully developed channel flow, periodic boundary conditions are prescribed along the streamwise and spanwise boundaries. Streamwise boundaries, inlet and outlet are paired, and spanwise boundaries, front and back are paired. The boundaries along the y direction are treated as solid walls. Except for velocity, all other quantities are initialised with a zero value. Momentum source is also provided as a pressure gradient to drive the flow. In OpenFOAM, momentum source can be provided by specifying the required bulk velocity.

The flow is characterized by a friction Reynolds number given by:

$$Re_\tau = \frac{u_\tau h}{\nu} \tag{4.1}$$

The target Re_τ is 290 for 10m/s case and 535 for 20 m/s case.

Velocity is initialised by choosing a parabolic profile and multiplying it with a random integer between 0 and 2 at each cell. the overview of boundary conditions is given below:

Table 4.2: Boundary conditions

Boundaries	**Inlet**	**Outlet**	**Wall**	**Front**	**Back**
Velocity	Periodic	Periodic	noSlip	Periodic	Periodic
Pressure	Periodic	Periodic	zeroGradient	Periodic	Periodic
SGS viscosity	Periodic	Periodic	zeroGradient	Periodic	Periodic

4.2 Results

The simulations are run until statistical convergence in the second order moments of the velocity is achieved. The time taken is approximately $1140\frac{h}{U_b}$ for 10 m/s case and $570\frac{h}{U_b}$ for 20 m/s case. Here, h is the channel half height and U_b is the bulk velocity.

4.2.1 Comparison of SGS models

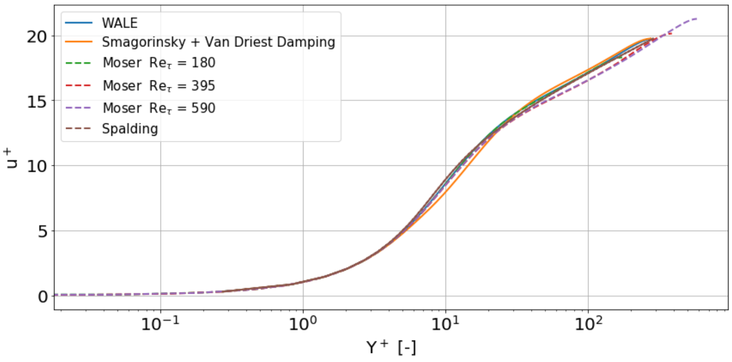

Figure 4.2: Dimensionless mean streamwise velocity compared for different SGS models

.

Figure 4.2 shows mean streamwise velocity normalised by the friction velocity. We can see that there is a slight under prediction of the mean velocity by the Smagorinsky model in the buffer layer. WALE model on the other hand predicts the mean velocity really well.

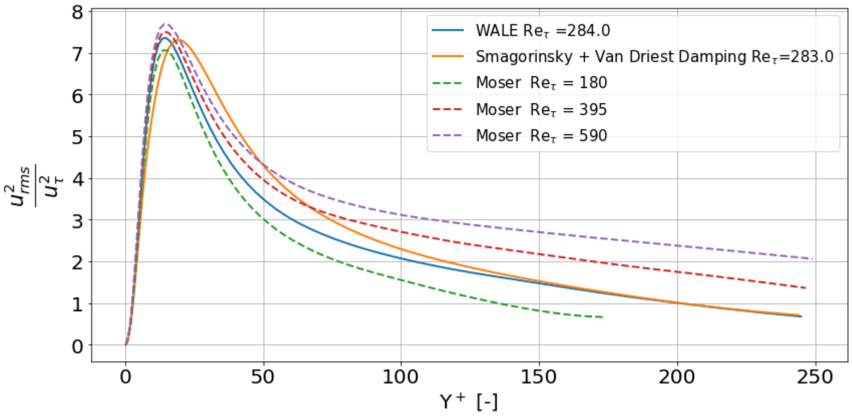

Figure 4.3: Dimensionless streamwise velocity variance compared for different SGS models

.

Figure 4.3 shows the streamwise velocity variance predicted by the SGS models. Smagorinsky model inaccurately predicts the peak and the location of the peak of the velocity variance when compared with the DNS results. WALE model on the other hand predicts both the peak and the location accurately. The accurate prediction of the location of peak is important for the accurate prediction of the coherent structures.

Figures 4.4 and 4.5 shows the wall normal and spanwise velocity variance respectively. In the wall normal velocity variance the inaccurate prediction by the Smagorinsky model can be attributed to the Van Driest damping used to damp the variance near the wall. This shows the inadequacy of the Smagorinsky model in modeling the SGS viscosity close to the wall. WALE model on the other hand predicts the behaviour of the variances well. Smagorinsky model inaccurately predicts the location of the peak of turbulent stresses. WALE model on the other hand predicts both the location and value of the peak turbulent stresses accurately. Note that the peak in v_{rms}^2 observed before the buffer layer is due to the addition of the Smagorinsky SGS kinetic energy to the value obtained from filtered fields.

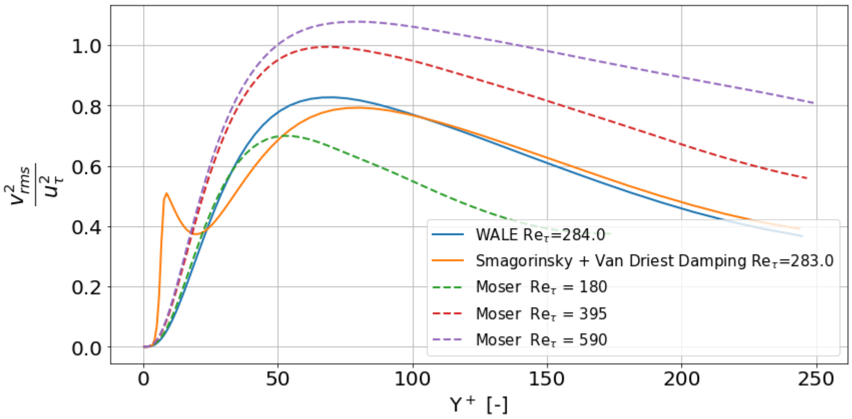

Figure 4.4: Dimensionless wall normal velocity variance compared for different SGS models

.

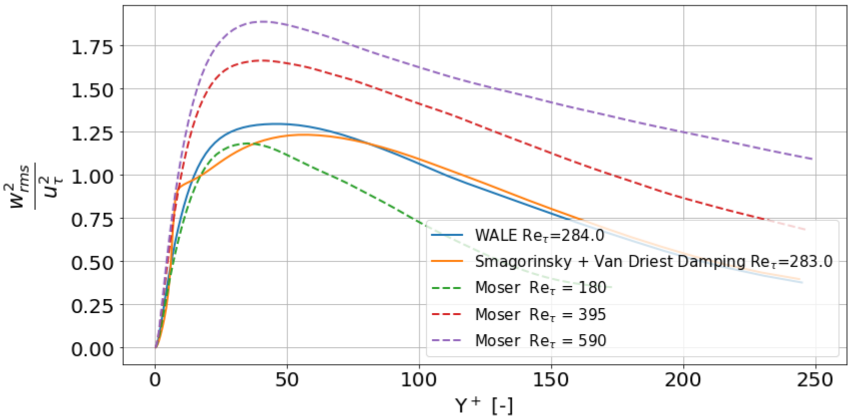

Figure 4.5: Dimensionless spanwise velocity variance compared for different SGS models

.

Figure 4.6 shows the Reynolds shear stress computed by the SGS models. We can see that Smagorinsky model under predicts the Reynolds shear stress. Accurate prediction of Reynolds shear stress is essential since this is the term responsible for the production of turbulent kinetic energy and accurate prediction of the coherent structures. WALE model on the other hand predicts the Reynolds shear stress well when compared to DNS data.

Figure 4.7 shows the total kinetic energy compared with modeled SGS kinetic energy. We can see that Smagorinsky model has a significant contribution from the SGS kinetic energy compared to the WALE model. WALE model almost completely resolves the total

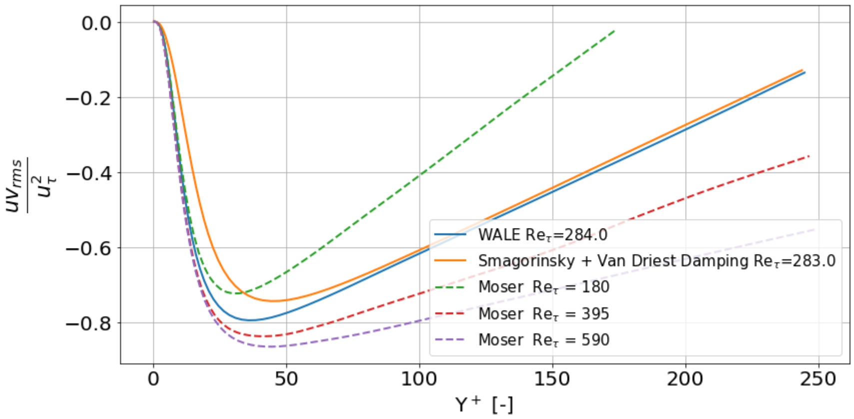

Figure 4.6: Dimensionless Reynolds shear stress compared for different SGS models

.

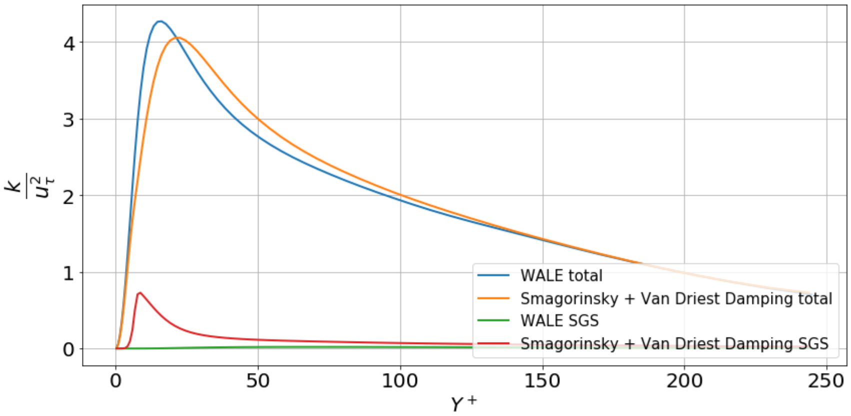

Figure 4.7: Dimensionless SGS kinetic energy compared for different SGS models

.

kinetic energy.

In order to properly elucidate the turbulent structures, proper resolution of these structures are necessary. Since WALE model resolves the kinetic energy better and also predicts the peak location accurately, WALE model is used as the SGS model in all the succeeding studies.

4.2.2 Time mean structure

The obtained velocity fields are averaged with time and along streamwise and spanwise directions. Obtained friction Reynolds number is 282 for 10m/s and 510 for 20 m/s case. This corresponds to friction velocity of 0.58 m/s for 10 m/s and 1.059 m/s for 20 m/s case.

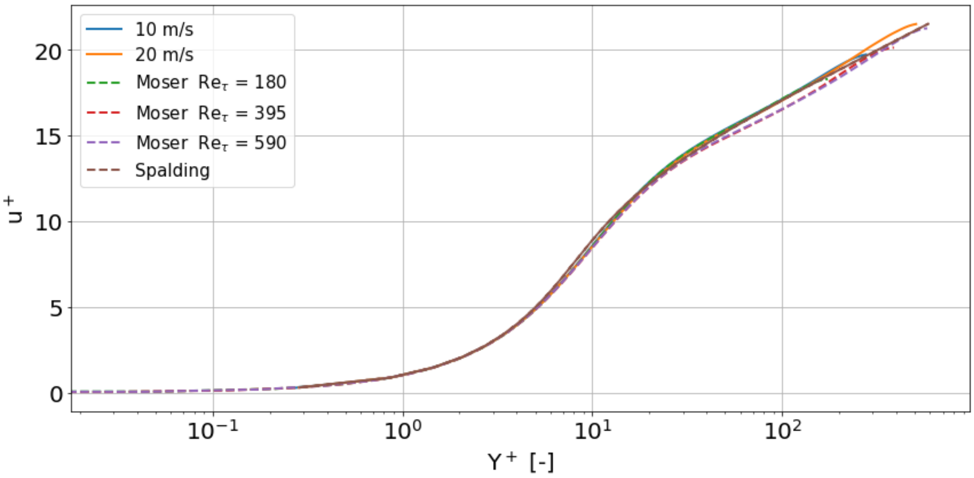

Figure 4.8: Dimensionless mean streamwise velocity

.

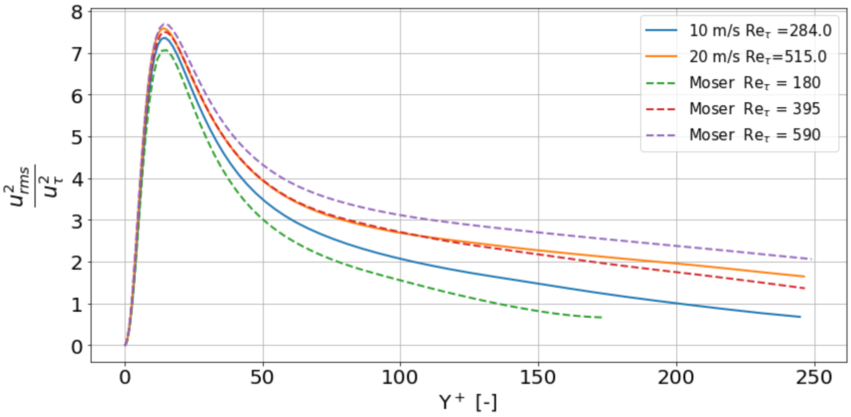

Figure 4.9: Dimensionless streamwise velocity variance

.

Figure 4.8 gives the mean streamwise velocities of 10 m/s and 20 m/s cases compared with the results from Moser et.al [24] and Spalding [34]. We can see that the mean velocity profiles are predicted well in the present study. Although there is a slight over prediction at the higher wall distances when compared to Spalding profile, the curves collapse really well onto the DNS results.

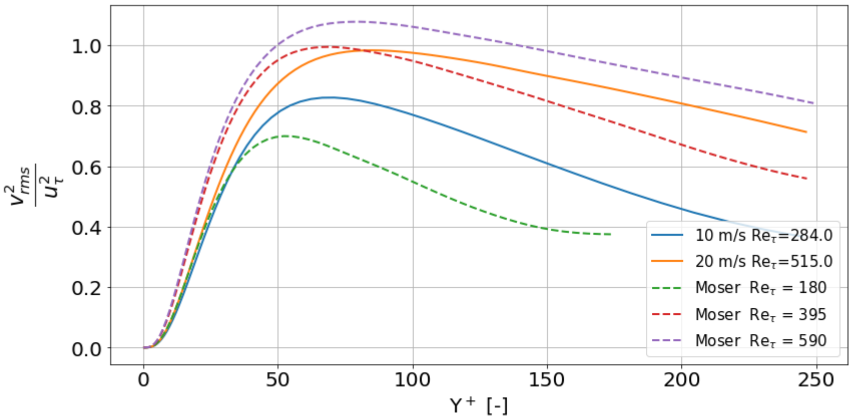

Figure 4.10: Dimensionless wall normal velocity variance

.

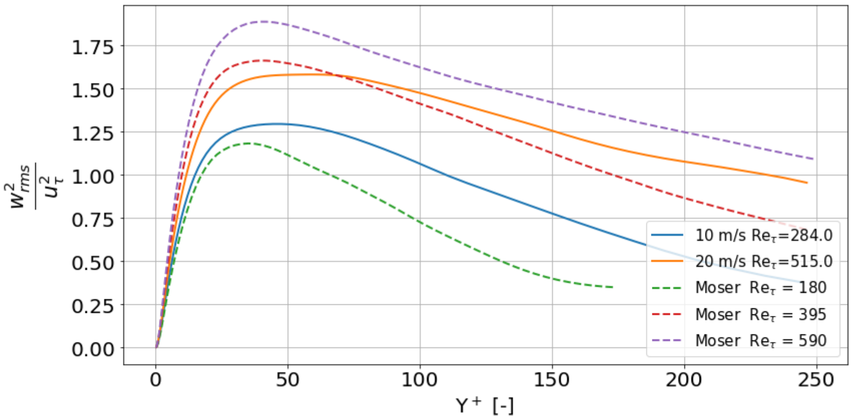

Figure 4.11: Dimensionless spanwise velocity variance

.

Figure 4.9 shows the comparison of dimensionless streamwise turbulent variance with Moser [24]. We can see that the peaks of the fluctuations and their locations are predicted well for 10 m/s case. There is a slight under prediction of the fluctuations in the 20 m/s case at $y^+ = 15$. However the fluctuations are predicted well away from the wall and towards the core region. This is also evident in figures 4.10, 4.11 and 4.12.

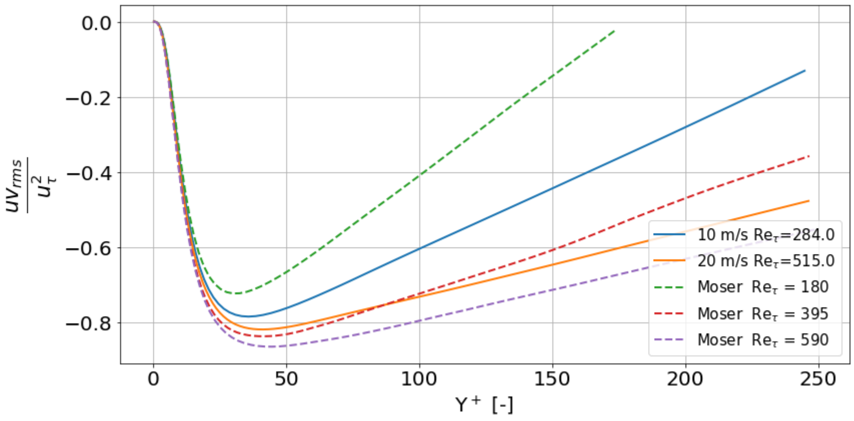

Figure 4.12: Dimensionless Reynolds shear stress

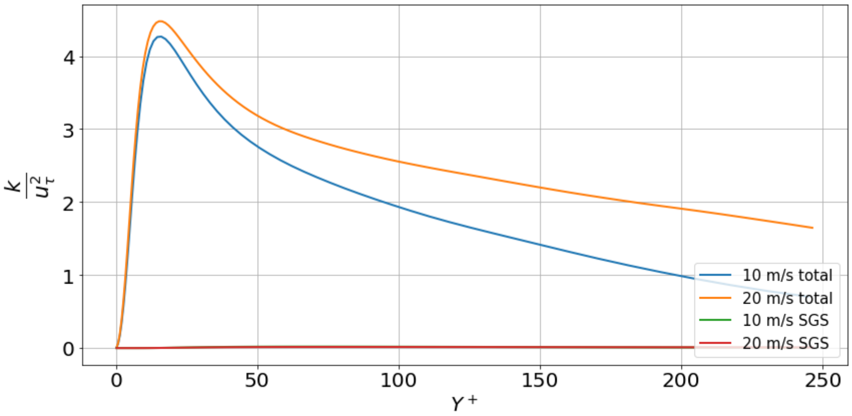

Figure 4.13: SGS kinetic energy

Figure 4.13 shows the total turbulent kinetic energy compared to SGS turbulent kinetic energy. As previously observed with WALE model, we can see that most of the turbulent kinetic energy is resolved for both 10 m/s case and 20 m/s case. There is an increase in the peak of turbulent kinetic energy at higher Reynolds number due to increased turbulent production. This increase in turbulent kinetic energy is more pronounced as we move away from the wall and into the core region.

4.2.3 Time resolved structure

After the convergence of the moments is achieved, data has been obtained every 5 $\frac{h}{Ub}$ times for a period of 650 $\frac{h}{Ub}$ for statistical analysis. The chosen time periods are such that the velocity fields obtained for the statistical analysis constitute an ensemble of velocity fields without any correlated data between each of the time instants.

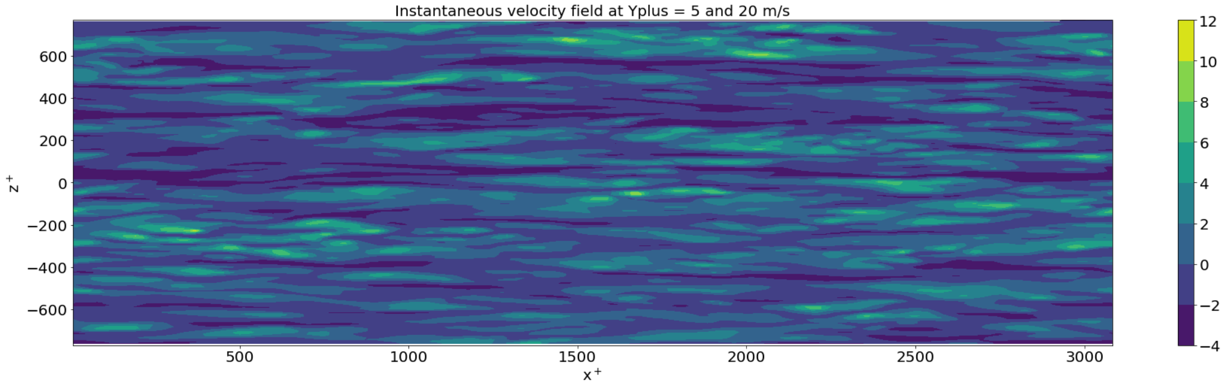

Figure 4.14: Instantaneous streamwise velocity fluctuations at y$^+$ = 5

.

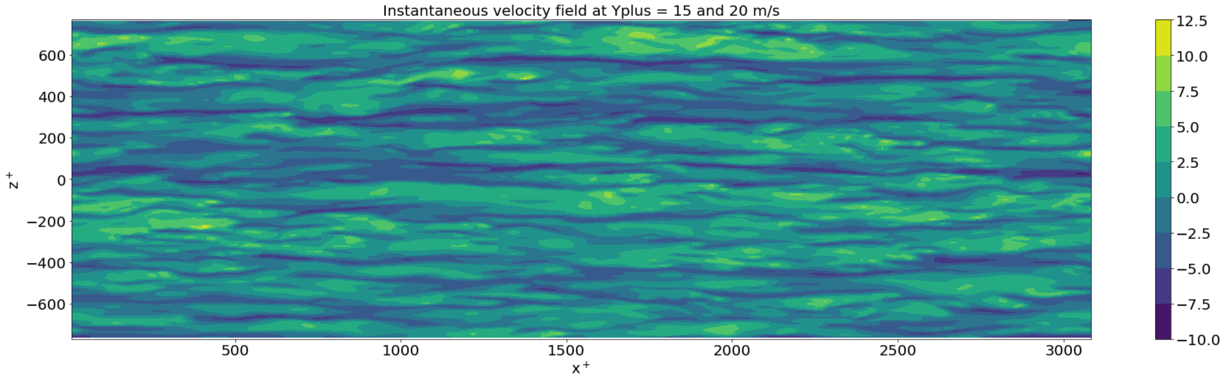

Figure 4.15: Instantaneous streamwise velocity fluctuations at y$^+$ = 15

.

Figures 4.14, 4.15 and 4.16 show the instantaneous turbulent fluctuations at y$^+$ of 5 (laminar sub layer), 15 (buffer layer) and 150 (logarithmic layer) . We can clearly see that laminar sub layer is not really laminar with the presence of distinct low and high speed

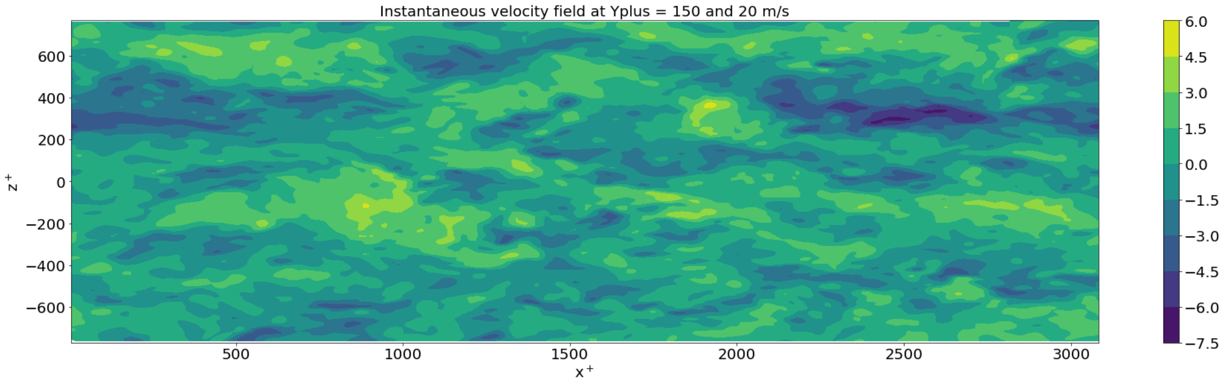

Figure 4.16: Instantaneous streamwise velocity fluctuations at y$^+$ = 150

.

streaks. We see that low speed streaks dominate in the laminar sub layer whereas their frequency decreases as we go into buffer layer away from the wall. The low speed streaks are also narrower and longer than the high speed streaks at both the wall distances. These streaks are responsible for the turbulent energy production in the buffer layer. These findings are in accordance with previous studies on the coherent structures in turbulent boundary layers. However, as we move away from the wall, we see that these structures lose their streaky appearance and become thicker in the spanwise direction. The streamwise extent of the turbulent structures is also lower compared to near wall regions.

Two point correlations of streamwise velocity fluctuations are performed to quantify the length scale observations made in the instantaneous velocity fields. Two point correlation of variables f$_1$ and f$_2$ at locations x$_1$ and x$_2$ respectively is given by :

$$C_{f_1,f_2}(x_1,x_2) = \overline{f_1(x_1)f_2(x_2)} \tag{4.2}$$

The two point correlations are normalized as follows :

$$R_{f_1,f_2}(x_1,x_2) = \frac{C_{f_1,f_2}(x_1,x_2)}{C_{f_1,f_2}(x_1,x_2)} \tag{4.3}$$

Conversely, we can choose a location x$_1$ and compute correlation based on separation vector r given by :

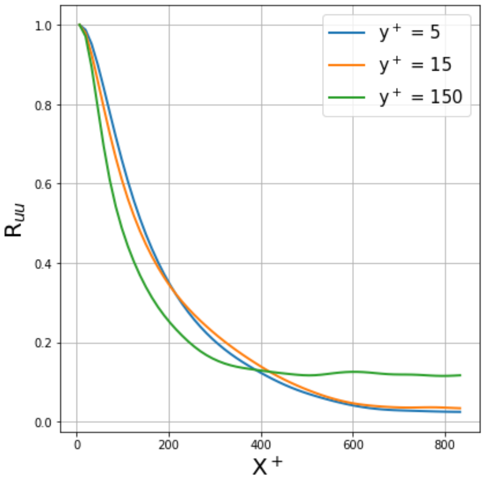

Figure 4.17: Longitudinal two point correlations of streamwise velocity fluctuations at different wall distances.

$$R_{f_1,f_2}(x_1, r) = \frac{\overline{f_1(x_1)f_2(x_1 + r)}}{(\overline{f_1(x_1)})(\overline{f_2(x_1)})} \tag{4.4}$$

where, r = x_2 - x_1 is the separation vector. If r is along the streamwise direction, we get longitudinal correlations and if r is along the spanwise direction, we get transverse correlations. All the correlations presented in this study are normalized accordingly.

Figure 4.17 shows the longitudinal two point correlations of streamwise velocity fluctuations at $y^+ = 5$, 15 and 150. We can see that the structures are longest at the near wall locations whereas they lose their streaky appearance at the higher wall distances. The minimum level of correlation is also higher at $y^+ = 150$ when compared to near wall regions. Figure 4.18 shows the transverse two point correlations of streamwise velocity fluctuations. The structures are narrower in the near wall region and become wider as we go towards core region. These results are consistent with the observations from instantaneous velocity fields.

Since most of the turbulent activity takes place in the buffer layer, we focus our study in this region.

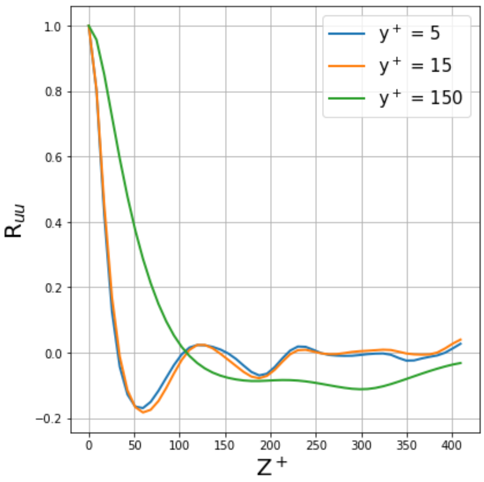

Figure 4.18: Transverse two point correlations of streamwise velocity fluctuations at different wall distances.

Chapter 5

2 degree Diffuser

5.1 Numerical setup

The computational domain of the diffuser is given below. The spanwise width of the domain is same as that of channel and the outlet channel is chosen long enough to avoid back-flow regions. The simulations are performed for the same inlet velocities as the channel case, that is, 10 m/s and 20 m/s.

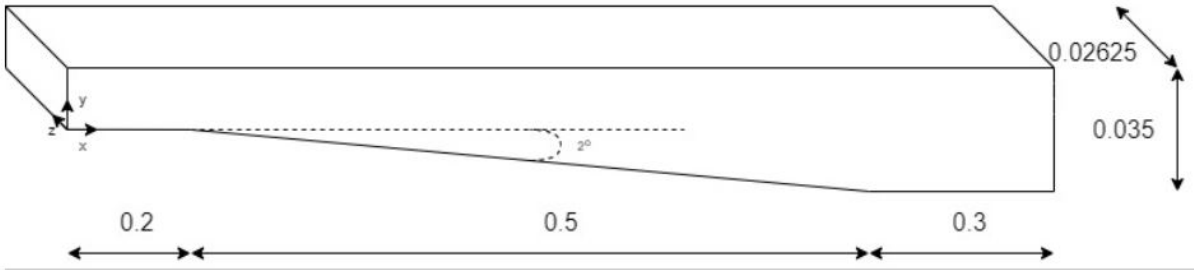

Figure 5.1: Computational domain for diffuser

.

The mesh resolution is chosen keeping in mind the computational resources available and the turbulent structure details obtained in the case of channel. Due to this the mesh resolution of the channel case cannot be translated into the diffuser case. Care has been taken not to decrease the spanwise resolution much as the accuracy of the simulation is strongly coupled to the spanwise resolution. Most of the resolution relaxation achieved is in the streamwise direction. The wall normal resolution is kept same as the channel case. The mesh and simulation settings are given below:

Table 5.1: Simulation and mesh settings for the diffuser

Cases	**10m/s**	**20m/s**
Cells	5.6 million	28 million
Wall y^+	0.6	0.6
Δx^+	38	38
Δz^+	15	15
Solution method	PIMPLE	PIMPLE
SGS model	WALE	WALE

5.1.1 Grid dependency of the WALE model

In order to check the influence of grid resolution on the performance of WALE model, a simulation of a 10m/s channel case is carried out with a coarser mesh. The mesh resolutions of the two meshes are given below:

Table 5.2: Mesh settings for the grid dependency study

Cases	**M1**	**M2**
Wall y^+	0.6	0.6
Δx^+	13	38
Δz^+	9	15

Figure 5.2 shows the mean streamwise velocities predicted by the two meshes. There is a slight over prediction of streamwise velocity in the logarithmic region. However, the

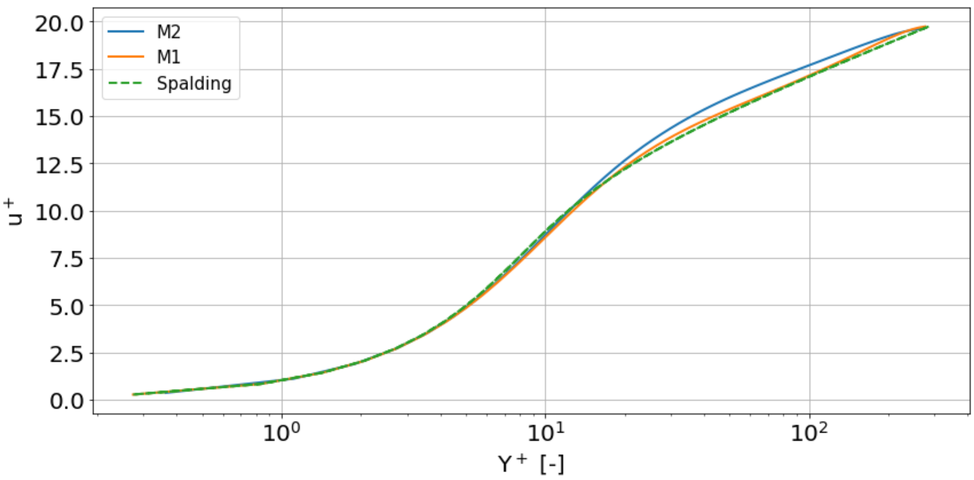

Figure 5.2: Dimensionless mean streamwise velocity comparison for two meshes

.

mean streamwise velocities are captured satisfactorily by the two meshes.

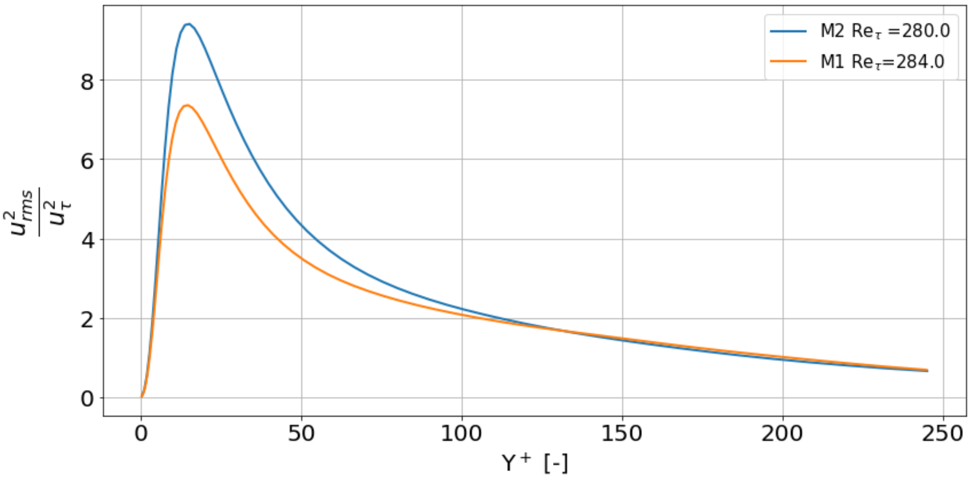

Figure 5.3: Dimensionless streamwise velocity variance comparison for two meshes

.

Figures 5.3, 5.4 and 5.5 shows the velocity variances of streamwise, wall normal and spanwise components respectively. There is an overestimation of the peak of streamwise velocity fluctuations in the coarser mesh. However, when it comes to wall normal and spanwise velocity fluctuations, there is an under prediction of the peak values. As seen in figure 5.6, the turbulent shear stress distribution is predicted accurately by both meshes.

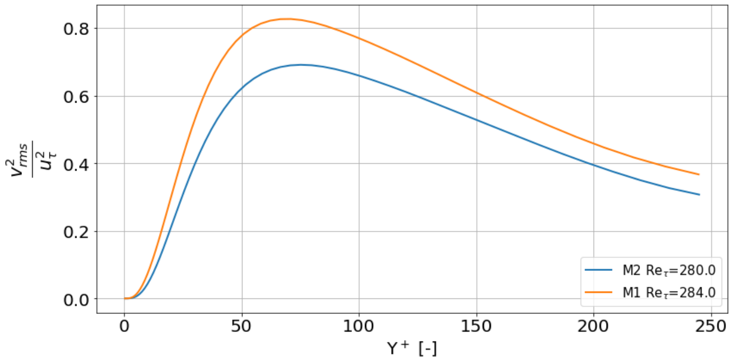

Figure 5.4: Dimensionless wall normal velocity variance comparison for two meshes

.

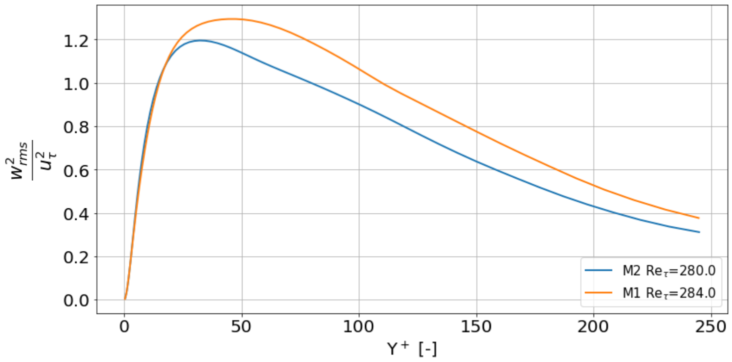

Figure 5.5: Dimensionless spanwise velocity variance comparison for two meshes

.

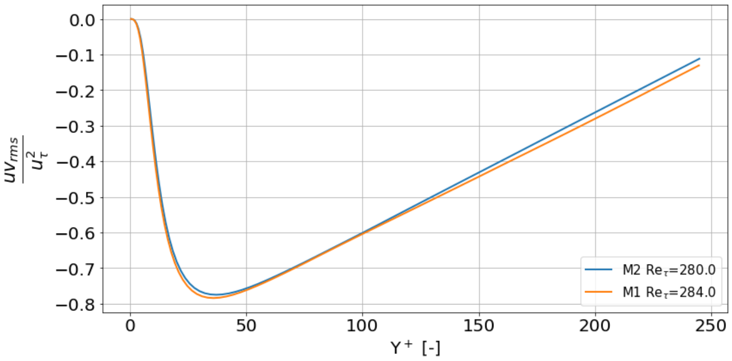

Figure 5.6: Dimensionless Reynolds shear stress comparison for two meshes

.

These results have also been observed in previous studies by Edmond [31] and Liang [32] where streamwise velocity variances are over estimated in the buffer layer. Edmond did not provide any reason for the over estimation and Liang reasoned it might be due to lower SGS viscosity and hence lower SGS dissipation predicted by the WALE model.

Statistical analysis similar to the channel case has been performed here as well to quantify the effects of mesh resolution on the resolution of coherent structures. Two point correlations of streamwise velocity are computed and compared for both the cases.

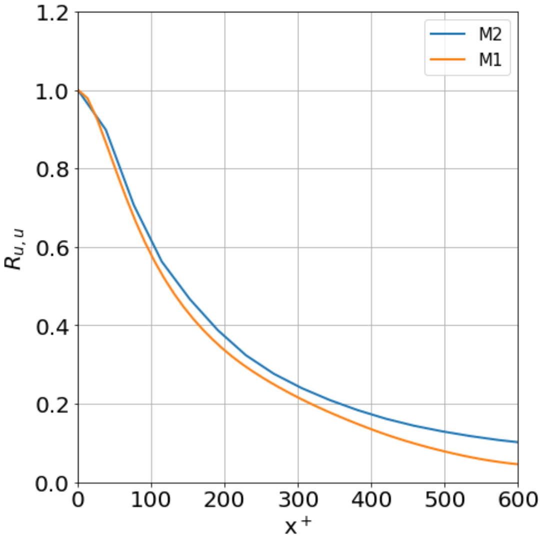

Figure 5.7: Two point correlations in the streamwise direction normalized by streamwise velocity variance

.

Figure 5.7 shows the normalized two point correlations along the streamwise direction. As we can see, M2 has slight over prediction in the length of the correlation when compared to M1. However this length is less than the grid spacing in streamwise direction of M2. Thus, we can imply that despite lower prediction in the SGS viscosity, the WALE model predicts the length of coherent structures relatively well. The same can be observed for the spanwise coherence in figure 5.8.

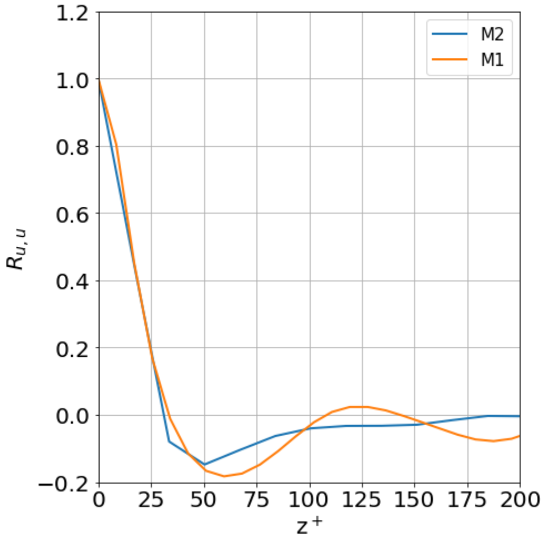

Figure 5.8: Two point correlations in the streamwise direction normalized by streamwise velocity variance

.

5.1.2 Initial and boundary conditions

It is essential to provide accurate velocity fields with proper coherence and second order moments at the inlet of the domain for the fidelity of the simulations. One way is to provide a recycling boundary condition at the inlet. However due to the over prediction of turbulent stresses by the WALE model for coarser resolutions, this can cause higher than normal turbulent fluctuations in the domain. Thus, the time dependent velocity profile from the precursor simulation is fed into the diffuser domain at the inlet. The precursor simulations for the cases are the channel simulations from the previous chapter.

Spanwise boundaries, front and back are periodic. The boundaries along the y direction are treated as solid walls. Advective boundary condition is chosen at the outlet so that any pressure waves are directed out of the domain. All the fields are initialised in the same way as the channel case. The overview of boundary conditions is given below:

Table 5.3: Boundary conditions

Boundaries	**Inlet**	**Outlet**	**Wall**	**Front**	**Back**
Velocity	Time dependent velocity	Advective	noSlip	Periodic	Periodic
Pressure	zeroGradient	Fixed value	zeroGradient	Periodic	Periodic
SGS viscosity	Periodic	Periodic	zeroGradient	Periodic	Periodic

5.2 Results

5.2.1 Time mean structure

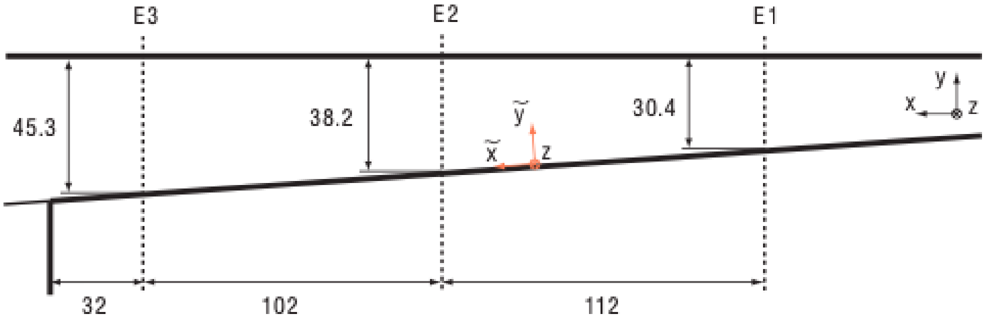

Figure 5.9: Definition of measurement locations by Eichler [6]

.

The obtained velocity fields are averaged across time and spanwise directions. The results are compared with Eichler at three downstream locations in the diffuser as shown in figure 5.9. Due to decreasing friction velocity along the downstream of expansion section, the mesh resolution is wall units also changes. These changes along with the predicted wall shear stress (assuming air at atmospheric pressure and temperatures) are given below :

Figures 5.10, 5.11 and 5.12 show mean velocity profiles of 2 degree diffuser compared with Eichler results. The mean velocity profile is over predicted in the E1 section. However when compared with the Spalding profile, the deviation is less. The prediction of mean

Table 5.4: Shear stress and resolutions predicted in the current study

Location	**Shear stress Eichler (Pa)**	**Shear stress current study (Pa)**	Δx^+	Δz^+
E1	0.6492	0.6183	26	10.5
E2	0.4130	0.4471	23	9.2
E3	0.2927	0.3542	20	8.2

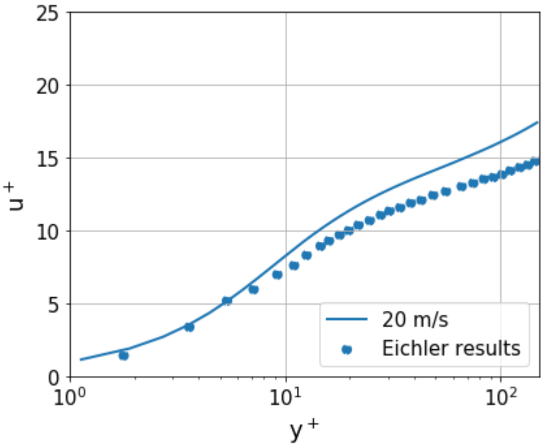

Figure 5.10: Mean streamwise velocity E1

.

velocity profile in E2 and E3 sections is better compared to the E1 section.

Figures 5.13, 5.14 and 5.15 show streamwise (u') and wall normal (v') variances normalized with friction velocity at the section. There is an over prediction in the peak of streamwise variance in the E1 section when compared with Eichler results. This over prediction can be attributed to the performance of WALE model in coarse meshes as discussed in the previous study. The peak of streamwise variances are predicted well in E2 and E3 locations owing to the finer resolution due to decrease in friction velocity along the downstream locations. However, the current study under predicts the streamwise variances at larger wall distances when compared with Eichler results. The wall normal variances are predicted well at all the three locations.

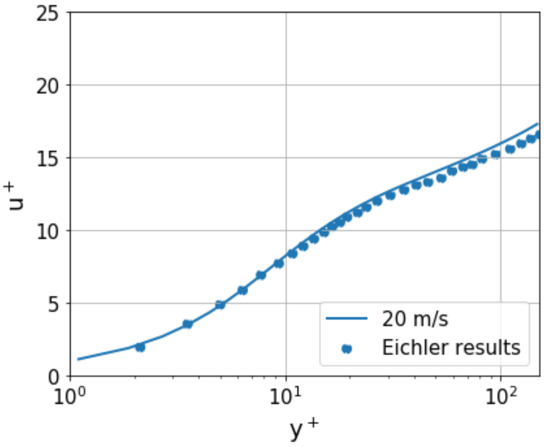

Figure 5.11: Mean streamwise velocity E2

.

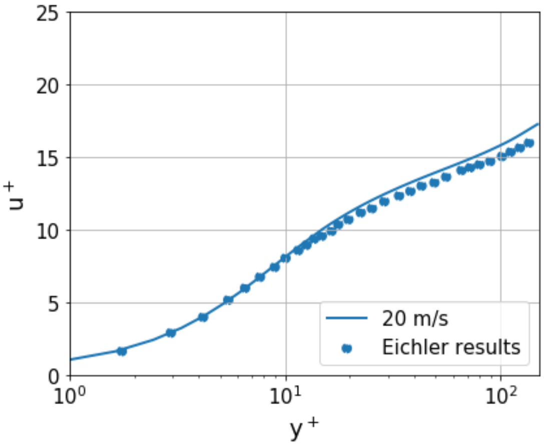

Figure 5.12: Mean streamwise velocity E3

.

5.2.2 Time resolved structure

After the convergence of the moments is achieved, data has been obtained at similar time intervals as the channel case. However, the time scale used for obtaining the ensemble fields is obtained by using half height and bulk velocity at the outlet section of the diffuser.

Figures 5.16, 5.17 and 5.18 show the instantaneous velocity fields at $y^+ = 15$ and three downstream locations. We can observe low and high speed streaks at all the downstream locations. Although there is not much difference in the dimensions of streaks at E1 and E2

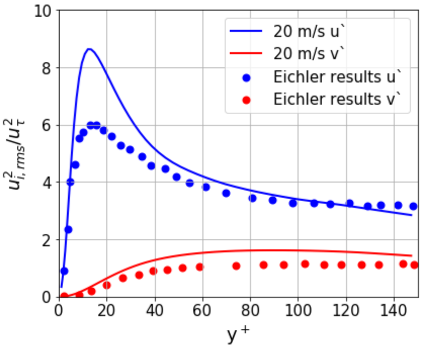

Figure 5.13: Velocity variances E1

.

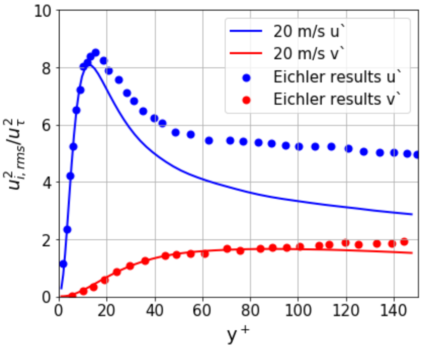

Figure 5.14: Velocity variances E2

.

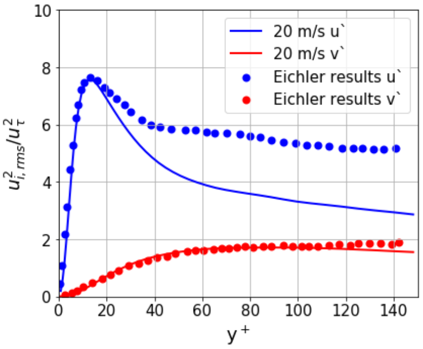

Figure 5.15: Velocity variances E3

.

locations, we find some differences at E2 and E3 locations. The streaks are enlarged at E3 location when compared with streaks at E2 location. Similar to channel case, we perform

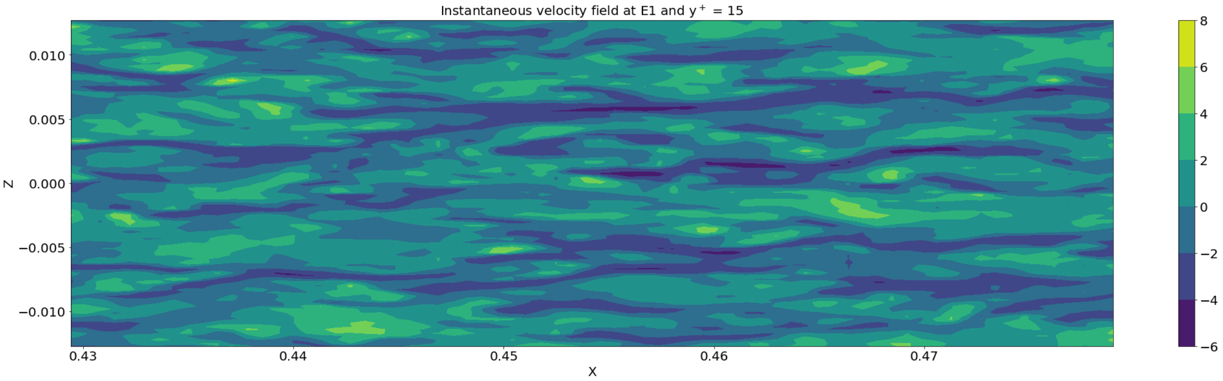

Figure 5.16: Instantaneous velocity fields at E1

.

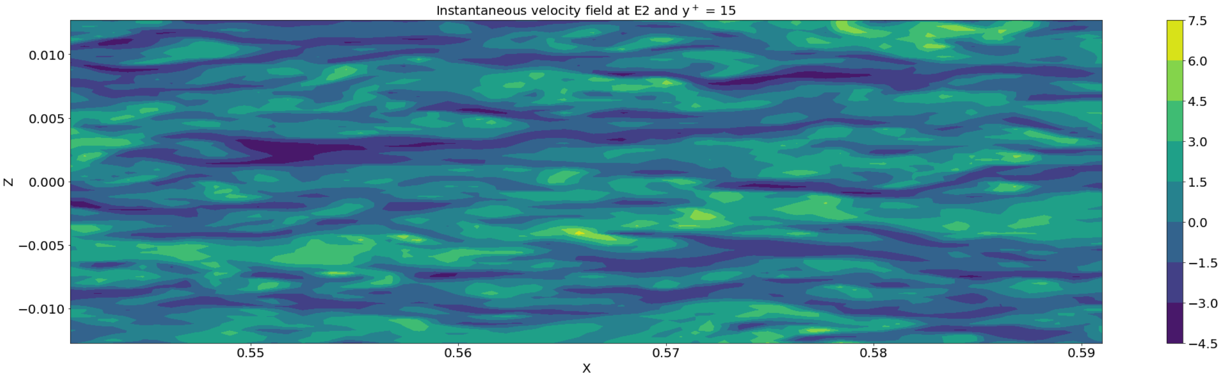

Figure 5.17: Instantaneous velocity fields at E2

.

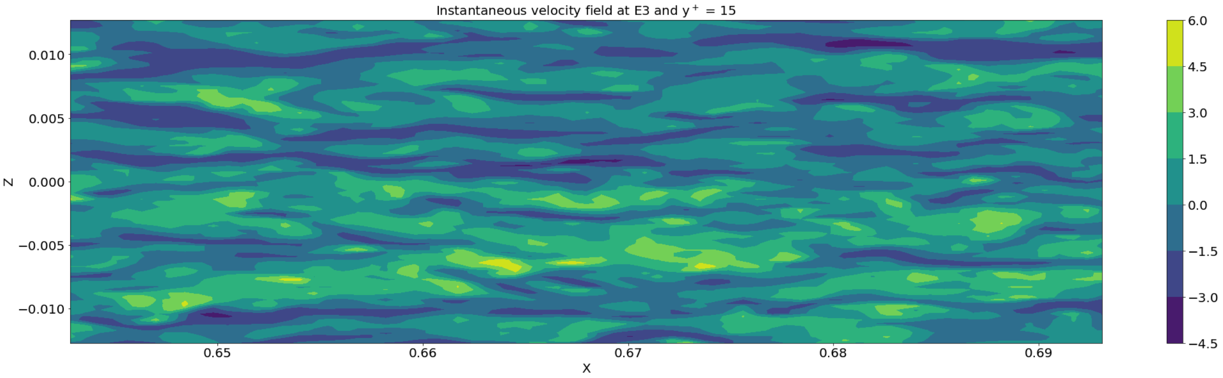

Figure 5.18: Instantaneous velocity fields at E3

.

two point correlations to describe the structure of these turbulent streaks.

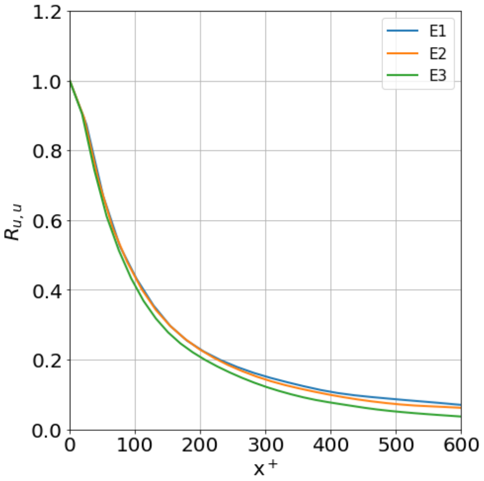

Figure 5.19: Longitudinal two point correlations of streamwise velocity fluctuations with length scale scaled in viscous units for the diffuser

.

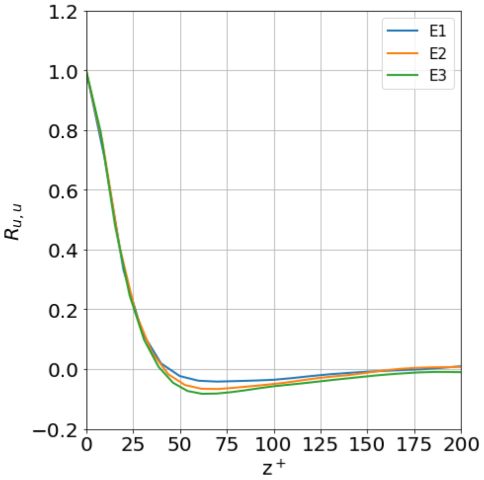

Figure 5.20: Transverse two point correlations of streamwise velocity fluctuations with length scale scaled in viscous units for the diffuser

.

Figure 5.19 gives the longitudinal correlation of streamwise velocity fluctuations at different downstream locations of the diffuser. We can see that when scaled with viscous units, the length of the streamwise correlation remains almost the same. The same behaviour is also observed in figure 5.20 of the spanwise correlation where there is no significant change in the spanwise width of the coherent structures.

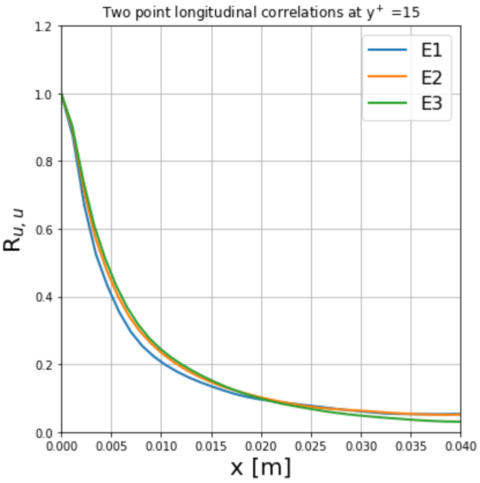

Figure 5.21: Longitudinal two point correlation of streamwise velocity fluctuations without any scaling

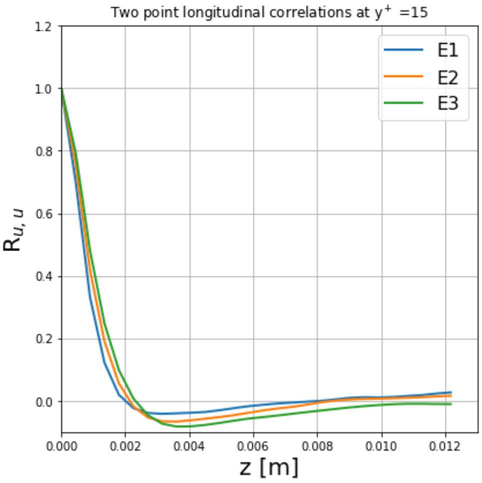

Figure 5.22: Transverse two point correlation of streamwise velocity fluctuations without any scaling

Figure 5.21 gives the longitudinal correlation of streamwise velocity fluctuations when the separation vector is not scaled by any units. We see that the structures are becoming longer in streamwise direction at downstream locations of the diffuser. There is no appreciable change in lengths of the structures at locations E2 and E3. Figure 5.22 gives the transverse correlation without any scaling in the spanwise length. We can observe that structures are becoming wider along the spanwise length at the downstream locations. Despite the changes in the length scale at different locations, the structures show a self similar behaviour when scaled in viscous units.

Chapter 6

Discussion

6.1 Comparison of turbulent structures in channel and diffuser flows

6.1.1 Cumulative distribution functions of low speed structures

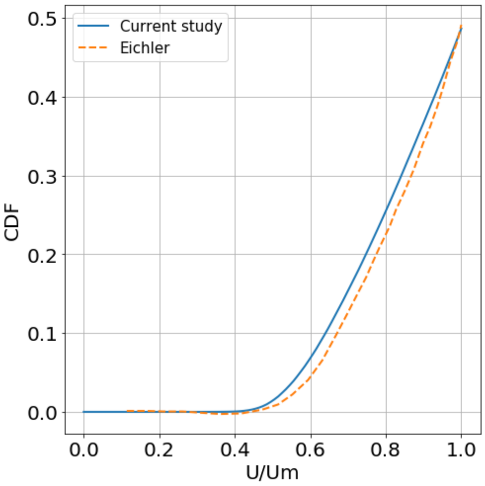

Figure 6.1: CDF of instantaneous velocity at $y^+ = 15$ for channel

.

In order to validate the turbulent structures obtained in the current study, cumulative distribution functions of low speed streaks are validated with Eichler results at $y^+ = 15$.

Figure 6.1 shows the low velocity streaks predicted by Eichler compared with the channel case. Although there is a slight over prediction in the intermediate strengths, the current study captured the distribution of streaks accurately.

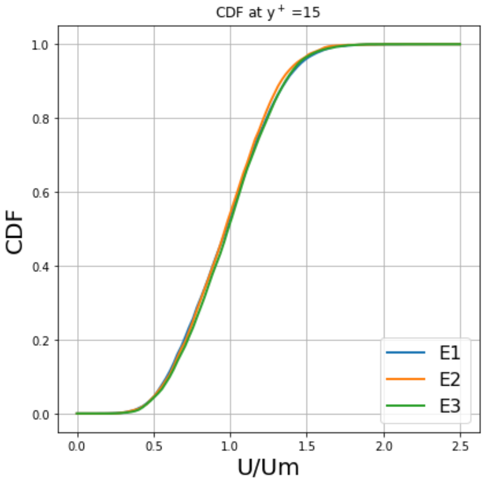

Figure 6.2: CDF of instantaneous velocity at y$^+$ = 15 for diffuser

.

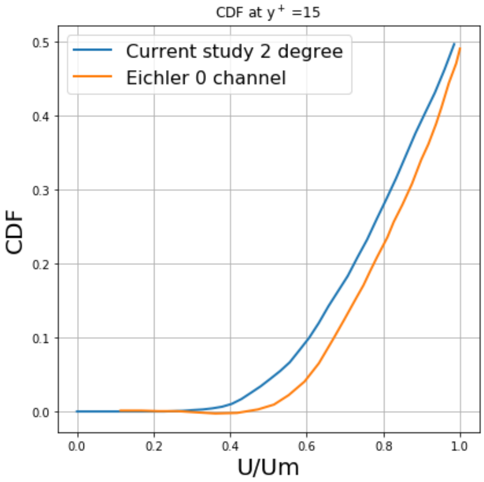

Figure 6.3: CDF of instantaneous velocity at y$^+$ = 15 for diffuser and channel

.

Figure 6.2 shows the CDF of instantaneous velocity normalized by mean velocity compared at different downstream locations. Similar to the observation by Eichler, there is no significant change in CDFs obtained at different downstream locations. Figure 6.3 shows the CDFs compared between channel and diffuser cases. We can see an increase in the low speed streak frequency when compared with the channel case. Frequency is increased across all the values of instantaneous velocity lower than the local mean velocity.

Since, the separation in the boundary layer tends to occur in these low speed streaks, the increased frequency can mean increased separation tendency of the boundary layer. Since wall flashback in confined flames occurs due to boundary layer separation, this increased frequency of low speed streaks indeed increases flashback propensity of the premixed flames.

6.1.2 Two-point Correlations of stream-wise velocity fluctuations

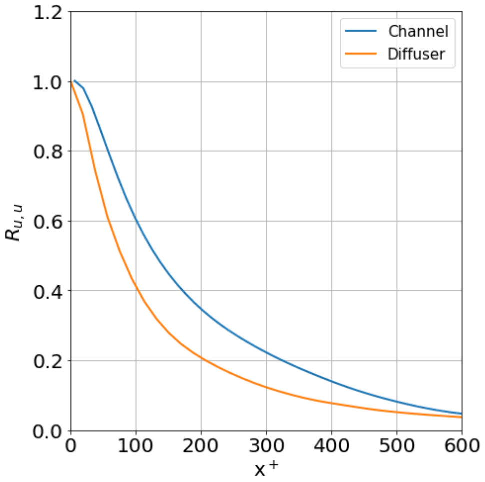

Figure 6.4: Two point correlations in the spanwise direction normalized by streamwise velocity variance for diffuser and channel

.

Figure 6.4 gives the streamwise correlations of the diffuser compared with the channel. We can notice that streamwise structures are significantly modified by the adverse pressure gradient. There is a reduction in the length of the coherent structures in the diffuser case compared to the channel case. This also in accordance with the observations in literature where in APG causes reduction in the streamwise extents of coherent structures.

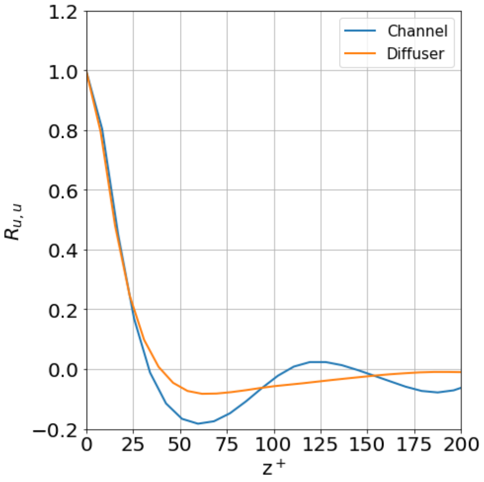

Figure 6.5: Two point correlations in the spanwise direction normalized by streamwise velocity variance for diffuser and channel

.

Considering the correlations in the spanwise direction, there is a slight increase in the width of the structures, when scaled in viscous units. The spacing between the streaks almost remains unchanged. Although, an increase in the spacing of the structures is expected, the strength of the pressure gradient in the diffuser is too low to observe any significant change.

Based on the preceding observations, we calculate the values for length scales of the coherent structures. The length scale in streamwise direction (x) is taken as the length at which streamwise coherence drops below 0.3. The length scale in the spanwise direction is the length at which coherence drops to 0. The spacing between streaks is taken as length scale corresponding to minimum coherence in the spanwise direction. We obtain following values for length scales :

Case	**Streamwise (L_x^+)**	**Spanwise (L_z^+)**	**Streak spacing (W^+)**
Channel	229	35	62
Diffuser	150	45	70

Table 6.1: Length scales of turbulent structures in different directions

6.2 Relative contribution of DL instability in channel and diffuser flows

In order to compare the relative influence on the DL instability, we compare frequencies of the turbulent structures of channel and diffuser case. The turbulent time scales are obtained by dividing streamwise length scale with the convection velocity. Kim and Hussain [14] estimated convection velocity of the streaks to be approximately 0.55*U_c where U_c is the centreline velocity. According to Taylor frozen turbulence hypothesis, the turbulent frequency is then given by :

$$\omega = u_{c,f}/L_x \tag{6.1}$$

where, ω is the turbulent frequency, $u_{c,f}$ is the convection velocity of the fluctuations and L_x is the streamwise length scale of the coherent structures. According to the equation above, we obtain following values of turbulent frequencies :

$$\omega_{channel} = 1428s^{-1} \tag{6.2}$$

$$\omega_{E1} = 978s^{-1} \tag{6.3}$$

$$\omega_{E2} = 750s^{-1} \tag{6.4}$$

$$\omega_{E3} = 590s^{-1} \tag{6.5}$$

Similar to the notation used by Chaudhuri [4], in order to show the difference in the propensity of DL instability, the growth rate associated with DL instability is normalized by turbulent frequency by :

$$\beta = \frac{\omega_{turb}}{\sigma_{DL}} \tag{6.6}$$

The chosen turbulent frequencies correspond to integral turbulent structures. If $\beta > 1$, the wrinkling due to DL instability is prevented and if $\beta < 1$, the DL instability is sustained.

We choose an equivalence ratio of 0.6 for this analysis. At this equivalence ratio, we obtain the following ratio of unburnt and burnt gas density calculated by Cantera [9] :

$$\varphi = 5.42$$

The corresponding value of Γ and cut-off wavelength λ_c is given by :

$$\Gamma = 1.2634$$

$$\lambda_c = 1.33 \ mm$$

The thermal flame thickness of the flame is defined by :

$$\delta_T = \frac{T_b - T_u}{max\left(\frac{dT}{dx}\right)} \tag{6.7}$$

Here, δ_T is the thermal flame thickness, T_b is the burnt gas temperature, T_u is the unburnt gas temperature and x is the progress variable. We take x as the coordinates of the 1D grid used in the cantera computations. We obtain the following value of δ_T :

$$\delta_T = 0.37 \ mm$$

We use diffusive flame thickness in the estimation of DL instability growth rate. We can construct effective diffusive flame thickness from thermal thickness according to the study by Blint [1]. The diffusive flame thickness is obtained by :

$$\delta_L = \frac{\alpha_{avg}}{S_L} \tag{6.8}$$

where, α_{avg} is average thermal diffusivity of the mixture given by :

$$\alpha = \frac{k_t}{\rho c_p} \tag{6.9}$$

where k_t is the thermal conductivity, ρ is the gas density and c_p is specific heat capacity of the mixture. According to Blint [1], the average ratio of thermal conductivty and specific heat of the mixture is given by :

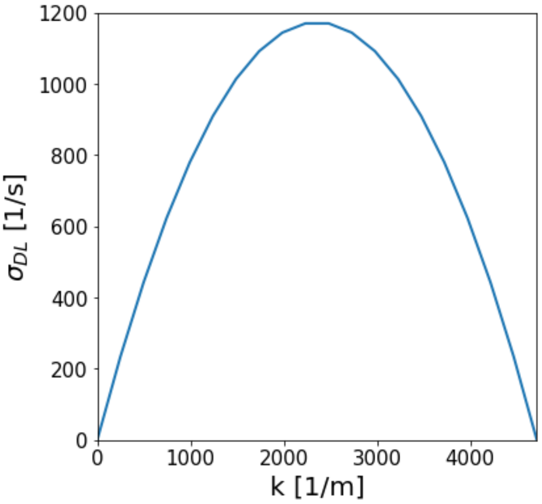

Figure 6.6: Growth rate of perturbations due to DL instability at equivalence ratio = 0.6. The fastest growing perturbations occur at k = k$_c$. The growth of perturations is suppressed at k > k$_c$ due to thermal stabilization.

$$\left(\frac{k_t}{c_p}\right)_{avg} = \rho_{avg} * S_L * \frac{\delta_T}{2} \tag{6.10}$$

We obtain following value of diffusive flame thickness :

$$\delta_L = 0.0583\ mm$$

Using the results obtained, we estimate the growth rate of perturbations due to DL instability. The growth rate of perturbations is shown in figure 6.6. We can see the fastest growing perturbations occur at k = k$_c$/2. The growth of perturbations are suppressed at k > k$_c$ due to thermal stabilization at shorter wavelength according to Bychkov [3].

Figure 6.7 shows the dependence of β with the perturbation wavelength for channel and E1, E2 and E3 locations of the diffuser. The lowest values of β for all cases occur at wavenumber k = k$_c$/2, which correspond to fastest growing perturbations. For the chosen equivalence ratio, β does not fall below one for the channel case. Hence, DL instability is suppressed due to turbulence. However, β goes below 1 for all the downstream locations of the diffuser. Thus, DL instability is sustained in all of the chose downstream locations.

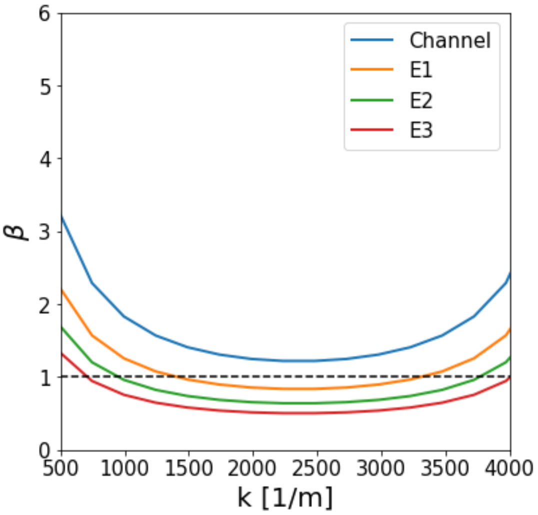

Figure 6.7: Turbulent frequencies normalized by DL instability growth rate. The black dotted line in the figure corresponds to $\beta = 1$. If β falls below this line, DL instability is sustained even in the presence of turbulence. However, if β stays above this line, turbulence inhibits the DL instability growth.

This increased propensity of DL instability can cause increased incidence of flashback since in the near wall regions, the DL instability can cause flow separation [10].

Chapter 7

Conclusions and recommendations

In the current study, detailed cold flow LES simulations are performed for the channel and 2 degree diffuser geometries from the Eichler [6] studies. The performances of WALE and Smagorinsky models are studied first to compare and choose the most suitable model. Then, the simulations are performed using the chosen model and are compared with the experimental results of Eichler. The details of time resolved turbulence are obtained and compared for both the channel and diffuser geometries. Finally, DL instability study is performed and relative influence of the instability on the flame propagation in the channel and diffuser geometries is characterized.

7.1 Conclusions

1. WALE model performed better than the Smagorinsky model in the prediction of time mean structure of turbulent boundary layers with accurate computation of location and size of the peak in turbulent fluctuations. However, WALE model overpredicts the turbulent fluctuations when using coarser mesh.

2. There is an increased frequency of incidence of low velocities in the diffuser case when compared to channel case. Since the separation of boundary layer occurs in these low velocity regions, this could be the cause of increased separation tendency

in the diffuser geometry observed in Eichler studies. Since flashback occurs due to separation of the boundary layer, this also means increased flashback propensity.

3. Integral length scales of turbulent structures are obtained with the aid of two point correlations in the buffer layer. The results show decreased coherent length scales in the diffuser case compared to channel case when scaled in viscous units. This observation is in accordance with various literature studies that document the decrease in the extent of streamwise coherence in the presence of adverse pressure gradient.

4. The effect of DL instability on the propagation of flame is higher in case of diffuser than the channel. This is due to the lower turbulent frequencies in the diffuser. This increase in the effect of DL instability can cause increase in the flame propagation speed. As discussed before, DL instability can cause separation of the boundary layer in the near wall regions. This is increased prevalence of DL instability can also be the cause of increased flashback propensity in the diffuser flow.

7.2 Recommendations

1. It is recommended to perform reactive flow simulations to get further details on the flame propagation in the diffuser geometries. In particular flame propagation speed differences in channel and diffuser geometries can give further insight into the effect of DL instability in the near wall regions.

2. In the current study, effect of quenching distance has been neglected in determining flashback propensity of the flame. Quenching distance plays an important role in the boundary layer flashback and must be studied in more detail

3. It is also recommended to perform simulations at higher reynolds numbers than the cases studied here. In the current study, there is no strong influence of low momentum regions in the logarithmic layer on the low velocity streaks in the near wall region.

Bross [2] reasoned that influence of low momentum regions in the log layer plays a very important role in the separation of boundary layer.

Bibliography

[1] Richard J Blint. The relationship of the laminar flame width to flame speed. *Combustion Science and Technology*, 49(1-2):79–92, 1986. 72

[2] Matthew Bross, Thomas Fuchs, and Christian J. Kähler. Interaction of coherent flow structures in adverse pressure gradient turbulent boundary layers. *Journal of Fluid Mechanics*, 873:287–321, 2019. xii, 28, 29, 77

[3] V Bychkov. Dynamics and stability of premixed flames. *Physics Reports*, 325(4-5):115–237, 2000. 20, 73

[4] Swetaprovo Chaudhuri, V'Yacheslav Akkerman, and Chung K. Law. Spectral formulation of turbulent flame speed with consideration of hydrodynamic instability. *Physical Review E*, 84(2), 2011. 21, 71

[5] II Contribution of Working Groups I and III to the Fifth Assessment Report of the Intergovernmental Panel on Climate Change. Climate change 2014: Synthesis report, 2014. xi, 1, 3

[6] Christian Thomas. Eichler. *Flame Flashback in Wall Boundary Layers of Premixed Combustion Systems*. Dr. Hut, 2011. xi, xii, xiii, 5, 7, 8, 9, 25, 59, 75

[7] A. Endres and T. Sattelmayer. Large eddy simulation of confined turbulent boundary layer flashback of premixed hydrogen-air flames. *International Journal of Heat and Fluid Flow*, 72:151–160, 2018. 8

[8] Aaron Endres and Thomas Sattelmayer. Numerical investigation of pressure influence on the confined turbulent boundary layer flashback process. *Fluids*, 4(3):146, 2019. 8

[9] David G. Goodwin, Raymond L. Speth, Harry K. Moffat, and Bryan W. Weber. Cantera: An object-oriented software toolkit for chemical kinetics, thermodynamics, and transport processes. `https://www.cantera.org`, 2018. Version 2.4.0. 12, 72

[10] A. Gruber, J. H. Chen, D. Valiev, and C. K. Law. Direct numerical simulation of premixed flame boundary layer flashback in turbulent channel flow. *Journal of Fluid Mechanics*, 709:516–542, 2012. xi, 8, 9, 74

[11] Alireza Kalantari, Nicolas Auwaijan, and Vincent Mcdonell. Boundary layer flashback prediction for turbulent premixed jet flames: Comparison of two models. *Volume 4A: Combustion, Fuels, and Emissions*, 2019. xi, 7

[12] Alireza Kalantari and Vincent Mcdonell. Boundary layer flashback of non-swirling premixed flames: Mechanisms, fundamental research, and recent advances. *Progress in Energy and Combustion Science*, 61:249–292, 2017. 7

[13] Alireza Kalantari, Elliot Sullivan-Lewis, and Vincent Mcdonell. Application of a turbulent jet flame flashback propensity model to a commercial gas turbine combustor. *Volume 4B: Combustion, Fuels and Emissions*, 2016. 7

[14] John Kim and Fazle Hussain. Propagation velocity of perturbations in turbulent channel flow. *Physics of Fluids A: Fluid Dynamics*, 5(3):695–706, 1993. 71

[15] C.K Law and C.J Sung. Structure, aerodynamics, and geometry of premixed flamelets, Jul 2000. xii, xii, xii, 15, 17, 18, 19

[16] Jin Lee, Seong Jae Jang, and Hyung Jin Sung. Direct numerical simulations of turbulent flow in a conical diffuser. *Journal of Turbulence*, 13, 2012. 29

[17] Joung-Ho Lee and Hyung Jin Sung. Structures in turbulent boundary layers subjected to adverse pressure gradients. *Journal of Fluid Mechanics*, 639:101–131, 2009. xii, 27, 28

[18] Bernard Lewis and Guenther Von Elbe. Stability and structure of burner flames. *The Journal of Chemical Physics*, 11(2):75–97, 1943. 6

[19] D. K. Lilly. A proposed modification of the germano subgrid-scale closure method. *Physics of Fluids A: Fluid Dynamics*, 4(3):633–635, 1992. 36

[20] Y.-C. Lin, S. Daniele, P. Jansohn, and K. Boulouchos. Turbulent flame speed as an indicator for flashback propensity of hydrogen-rich fuel gases. *Volume 1B: Combustion, Fuels and Emissions*, 2013. 7

[21] A.n. Lipatnikov and J. Chomiak. Effects of premixed flames on turbulence and turbulent scalar transport. *Progress in Energy and Combustion Science*, 36(1):1–102, 2010. xi, 9, 10

[22] George H. Markstein. *Nonsteady flame propagation.* Pergamon, 1964. 17

[23] Moshe Matalon. Intrinsic flame instabilities in premixed and nonpremixed combustion. *Annual Review of Fluid Mechanics*, 39(1):163–191, 2007. 20

[24] Robert D. Moser, John Kim, and Nagi N. Mansour. Direct numerical simulation of turbulent channel flow up to re=590. *Physics of Fluids*, 11(4):943–945, 1999. xii, 23, 24, 45, 46

[25] F. Nicoud and F. Ducros. Subgrid-scale stress modelling based on the square of the velocity gradient tensor. *Flow, Turbulence and Combustion*, 62(3):183–200, 1999. 36

[26] Frans T.M. Nieuwstadt, Jerry Westerweel, and Bendiks J. Boersma. *Turbulence Introduction to Theory and Applications of Turbulent Flows.* Springer International Publishing, 2018. xii, 21, 22, 26

[27] Norbert Peters. *Turbulent combustion.* Cambridge University Press, 2009. xi, 12, 13, 14

[28] Thierry Poinsot and D. Veynante. *Theoretical and numerical combustion.* T. Poinsot, D. Veynante, 2012. xi, xi, xii, 10, 14, 16, 20

[29] Stephen B. Pope. *Turbulent flows.* Cambridge University Press, 2019. 25

[30] S K Robinson. Coherent motions in the turbulent boundary layer. *Annual Review of Fluid Mechanics*, 23(1):601–639, 1991. 23

[31] Edmond Shehadi. Large eddy simulation of turbulent flow over a backward-facing step. 2018. 57

[32] Liang Shi. Influence of subgrid scale models on the buffer sublayer in channel flow. *arXiv preprint arXiv:1708.09531*, 2017. 57

[33] J. Smagorinsky. General circulation experiments with the primitive equations. *Monthly Weather Review*, 91(3):99–164, 1963. 35

[34] D. B. Spalding. A single formula for the "law of the wall". *Journal of Applied Mechanics*, 28(3):455–458, 1961. 23, 45

[35] Carlos Sanmiguel Vila, Ramis Örlü, Ricardo Vinuesa, Philipp Schlatter, Andrea Ianiro, and Stefano Discetti. Adverse-pressure-gradient effects on turbulent boundary layers: Statistics and flow-field organization. *Flow, Turbulence and Combustion*, 99(3-4):589–612, 2017. xii, 26, 27

[36] James M. Wallace, Helmut Eckelmann, and Robert S. Brodkey. The wall region in turbulent shear flow. *Journal of Fluid Mechanics*, 54(1):39–48, 1972. xii, 24, 25

Appendix A

Python code for calculating flame properties used in DL instability study.

```
# -*- coding: utf-8 -*-

import cantera as ct
import numpy as np
phi = [0.6]
omega = [1428,980,750,590]



flamespeed = np.ones(len(phi))
varphi = np.ones(len(phi))
thermalthick = np.ones(len(phi))
diffuthick = np.ones(len(phi))
cutoffwave = np.ones(len(phi))
cutoffnumber = np.ones(len(phi))
growthrate = np.ones(len(phi))
urmst = np.ones(len(phi))
```

```
urms = (8*0.3*0.3)**0.5
Tin = 300
p = 1*10**5



width = 0.03  # m
loglevel = 1  # amount of diagnostic output (0 to 8)
numb = 1500

for i in range(len(phi)):
    gas = ct.Solution('gri30.xml')

    reactants = 'H2:'+str(2*phi[i])+', O2:1, N2:3.76'

    gas.TPX = Tin, p, reactants

    gas.transport_model = 'Multi'

    k = gas.thermal_conductivity
    rho = gas.density_mass
    cp = gas.cp_mass
    alpha = k/(rho*cp)

    # Set up flame object
    f = ct.FreeFlame(gas, width=width)
    f.set_refine_criteria(ratio=3, slope=0.06, curve=0.12)
    #f.show_solution()

    # Solve with mixture-averaged transport model
    #f.transport_model = 'Mix'

    #f.solve(loglevel=loglevel, auto=True)
```

```
    # Solve with the energy equation enabled
    #f.save('h2_adiabatic.xml', 'mix',\
    #  'solution with mixture-averaged transport')
    #f.show_solution()
    #print('mixture-averaged flamespeed = {0:7f} m/s'.format(f.u[0]))

    # Solve with multi-component transport properties
    f.transport_model = 'Multi'
    #f.solve(loglevel) # don't use 'auto' on subsequent solves
    f.solve(loglevel=loglevel, auto=True)
    #f.show_solution()
    #print('multicomponent flamespeed = {0:7f} m/s'.format(f.u[0]))
    #f.save('h2_adiabatic.xml','multi',\
    # 'solution with multicomponent transport')

    ## write the velocity, temperature, density,
    ## and mole fractions to a CSV file
    #f.write_csv('h2_adiabatic.csv', quiet=False)
    flamespeed[i] = f.u[0]

    varphi[i] = f.density[0]/f.density[-1]

    x = f.flame.grid

    dx = x

    for ij in range(len(dx)-1):
        dx[ij] = x[ij+1] - x[ij]

    dx[-1] = dx[-2]

    dT = numpy.ones(len(f.u))

    for ii in range(len(dT)-1):
```

```
        dT[ii] = f.T[ii+1]-f.T[ii]

    dT[-1] = 0

    dTdx = dT/dx

    thermalthick[i] = (f.T[-1]-f.T[0])/max(dTdx)

    diffuthick[i] = (thermalthick[i]/2)/(0.5+0.5*varphi[i])

    Gamma = (varphi[i]/(varphi[i]+1))*(((varphi[i]+1-(1/varphi[i]))**0.5)-1)

    cutoffwave[i] = (1+varphi[i]*np.log(varphi[i])*((varphi[i]+1+2*Gamma)/(varphi[i]-1)**2))*(diffuthick[i]*np.pi*(varphi[i]-1)/(Gamma*(varphi[i]+1-1/varphi[i])**0.5))

    cutoffnumber[i] = 2*np.pi/cutoffwave[i]

    k = np.linspace(0,cutoffnumber[i],20)

    fastestwave = 2*cutoffwave[i]

    fastestnumber = 2*np.pi/fastestwave

    number = fastestnumber

    wave = 2*np.pi/number

    growthrate = np.asarray([Gamma*flamespeed[i]*num*(1-num/cutoffnumber[i]) for num in k])

    urmst[i] = 0.75*Gamma*flamespeed[i]
```